Mesoscale Eddy-Induced Sharpening of Oceanic Tracer Fronts and its Parameterization

Yueyang Lu*, RSMAES
Igor Kamenkovich, RSMAES

Mesoscale Eddy-Induced Sharpening of Oceanic Tracer Fronts and its Parameterization

Yueyang Lu[1] † and Igor Kamenkovich[1]

[1]Rosenstiel School of Marine, Atmospheric, and Earth Science, University of Miami, Miami, Florida

(Received xx; revised xx; accepted xx)

Oceanic fronts are ubiquitous and important features that form and evolve due to multiscale oceanic and atmospheric processes. For example, large-scale temperature and tracer fronts along the eastward extensions of the Gulf Stream and Kuroshio currents play key roles in the regional ocean environment and climate. The fronts cannot be realistically simulated by numerical models at spatial resolutions that do not resolve the oceanic mesoscale. This numerical study examines the relative importance of large-scale and mesoscale currents ("eddies") in the front formation and evolution. Using an idealized model of the double-gyre system on both eddy-resolving and coarse-resolution grids, we demonstrate that the effect of eddies is to sharpen the large-scale front, whereas the large-scale current counteracts this effect. The eddy-driven frontogenesis is further described in terms of a recently proposed framework of generalized eddy-induced advection, which represents all those eddy effects on tracers that are not due to eddy-induced mass fluxes and are traditionally parameterized by isopycnal diffusion. In this study the generalized advection is represented using an effective eddy-induced velocity (EEIV), which is the speed at which eddies move tracer contours. The advantage of this formulation is that the frontal sharpening can be readily reproduced by EEIVs, whereas it cannot be modeled as a diffusive process. A proposed closure ("parameterization") for EEIV based on large-scale properties shows promise in representing frontogenesis in coarse-resolution simulation. This study demonstrates advantages of using an advective rather than diffusive framework for representing eddy effects in coarse-resolution models.

Key words:

1. Introduction

Fronts, characterized by narrow bands of enhanced gradients of physical and biogeochemical tracers such as temperature, dissolved carbon and nutrients, are ubiquitous in the upper ocean. The width of ocean fronts can range from a few meters to tens of kilometers (McWilliams 2021), and processes at various spatial scales play a role in front formation and evolution (Belkin *et al.* 2009). Fronts can facilitate the transfer of the tracers from the surface to the ocean interior and play an important role in the climate and ocean ecological systems

† Email address for correspondence: yueyang.lu@miami.edu

(D'Asaro *et al.* 2011; Ferrari 2011; Lohmann & Belkin 2014). The fronts associated with strong large-scale currents, such as western boundary current extensions and the Antarctic Circumpolar Current, can have length extending for hundreds of kilometers and are of particular importance. These large-scale fronts can act as dynamical barriers to cross-frontal transport and mixing (Rypina *et al.* 2011, 2013) and impact the lower troposphere and mid-latitude climate (Small *et al.* 2008; Minobe *et al.* 2008; Seo 2023). The goal of this study is to examine the role of ocean mesoscale eddies [length scale of $O(10–100)$ km; "eddies" hereafter] in the evolution of large-scale temperature and tracer fronts associated with the eastward extensions of western boundary currents.

Oceanic mesoscale eddies pervade the vicinity of large-scale currents and can influence the fronts in several important ways. Baroclinic instability of these currents, which is one of the main mechanisms for eddy generation, can be expected to weaken the vertical shear and density fronts (Pedlosky 1987; Vallis 2017). On the other hand, eddies can have a straining effects that generate and sharpen the associated fronts (e.g., Berloff 2005; Waterman & Jayne 2011). Oceanic components in modern climate models, however, do not fully resolve mesoscale eddies (Meijers 2014; Hewitt 2020), which leads to biases in the simulated ocean state. For example, non-eddy-resolving models simulate much weaker sea surface temperature (SST) fronts in the Gulf Stream extension than is seen in eddy-resolving ocean models or observations (Kirtman 2012; Parfitt *et al.* 2016; Siqueira & Kirtman 2016). The biases in the SST front in these simulations can impact the atmospheric temperature front (Parfitt *et al.* 2016), storm tracks (Small *et al.* 2014), and climate variability (Kirtman 2012).

Mesoscale eddies can affect tracer fronts through multiple processes: the dynamic feedback of eddies on the large-scale current, the eddy-induced mass fluxes, and the eddy stirring and mixing. Most of previous studies have focused on understanding and parameterization of the first two processes. The dynamic effect of eddies refers to the eddy stirring of momentum (Waterman *et al.* 2011) and potential vorticity (PV; Berloff 2005; Waterman & Jayne 2011; Mana & Zanna 2014; Bachman *et al.* 2017; Ryzhov & Berloff 2022), which acts as both dissipation and a driving force for the large-scale current, which in turn advects the tracers and influences the fronts. Shevchenko & Berloff (2015) discussed this dynamic eddy effect on the PV front and found weaker fronts along the eastward jet extension in a quasi-geostrophic model at lower horizontal resolutions. The second effect, eddy-induced mass transport, is equivalent to an eddy-induced tracer advection and is commonly parameterized by the Gent–McWilliams framework (e.g. Gent & McWilliams 1990; Gent *et al.* 1995) that flattens isopycnals. This effect has been extensively studied and recent efforts mostly focus on advancing the GM parameterization (e.g. Grooms 2016; Grooms & Kleiber 2019; Bachman 2019; Bachman *et al.* 2020).

This study focuses on the third process, which is the most direct effect of eddies on tracers. It is traditionally treated as isotropic eddy-induced diffusion (Redi 1982). However, several recent studies have revealed the importance of its anisotropic diffusive (Bachman *et al.* 2015, 2020; Kamenkovich *et al.* 2021; Haigh *et al.* 2021*a*; Zhang & Wolfe 2022; Kamenkovich & Garraffo 2022) and advective (Haigh *et al.* 2021*b*; Lu *et al.* 2022) properties for tracer distributions. Most importantly, several studies of eddy diffusion demonstrate persistent up-gradient (negative) diffusion, which implies a mechanism of tracer filamentation and frontal sharpening ("frontogenesis"). Practical implementation of the up-gradient diffusion, however, leads to numerical instability, and negative diffusion conflicts with the analogy between turbulent and molecular diffusive mixing. The eddy-induced advection, in contrast, can be an appropriate model for the large-scale frontal development because the frontogenesis is essentially an advective process (McWilliams 2021). In addition, the transport barriers associated with the fronts are assumed to result from the joint action of the large-scale and eddy advections (Berloff *et al.* 2009; Kamenkovich *et al.* 2019). The advective formulation has

Parameter	Value	Description
$L_x \times L_y$	3840×3840 km	Horizontal domain dimensions
$\Delta x, \Delta y$	3.75 km	Horizontal grid spacing
H_1, H_2, H_3	(0.3, 0.7, 3) km	Initial isopycnal layer thicknesses
f_0	4.4×10^{-5} s^{-1}	Coriolis parameter at the southern boundary
β	2×10^{-11} m^{-1} s^{-1}	Meridional gradient of Coriolis parameter
ρ_0	1035 kg m^{-3}	Reference density
ν	100 m^2 s^{-1}	Laplacian horizontal viscosity
g	9.8 m s^{-2}	Gravity
g'	(0.01, 0.0003) m s^{-2}	Reduced gravities at the upper interface of layer $k = 2, 3$
C_d	0.003	Linear bottom drag coefficient
$\lvert\boldsymbol{u}_*\rvert$	0.1 m s^{-1}	Near-bottom velocity magnitude
τ_0	0.22 N m^{-2}	Wind stress amplitude
r	2×10^{-8} s^{-1}	Relaxation rate for the upper layer thickness
κ_{tr}	100 m^2 s^{-1}	Background isopycnal tracer diffusivity

Table 1: List of parameters used in the high-resolution model.

a clear advantage over the diffusive framework in this regard. For example, a perfect barrier naturally results from the full cancellation between the large-scale and eddy-induced velocity (zero "residual velocity"), while the barrier cannot be guaranteed for an arbitrary tracer if the effects of eddies are diffusive. Recently, Lu *et al.* (2022) has proposed a generalized eddy-induced advection to quantify the direct eddy effects, and used it to successfully reproduce the eddy-induced stirring and dispersion in a high-resolution model. This study will further advance this approach, and will examine the extent to which the stirring effects of eddies on a large-scale front can be modeled by eddy-induced advection and be parameterized in terms of large-scale quantities.

The paper is organized as follows. Section 2 describes the ocean models used in this study. Section 3 derives the tracer eddy forcing that includes the effects of eddies on a large-scale front, the frontogenesis equation and the generalized advective model of the eddy forcing. Section 4 examines the eddy effects on the front via the sensitivity experiments and analysis of the equation. Section 5 discusses performance of the tracer simulations with the eddy-induced advection. Section 6 offers conclusions.

2. Model

2.1. *Primitive equation ocean model*

We use the Modular Ocean Model version 6 (MOM6, Adcroft 2019) to solve the adiabatic shallow-water equations in a square basin with flat bottom. The model represents a wind-driven mid-latitude, double-gyre ocean circulation in the Northern Hemisphere, whose setup is motivated by Cooper & Zanna (2015). The model has three stacked isopycnal layers with a free surface. Key parameters are summarized in table 1.

The momentum and continuity equations in layer k ($k = 1, 2, 3$ with $k = 1$ denoting upper layer) are

$$\frac{\partial \boldsymbol{u}_k}{\partial t} + \frac{f+\zeta_k}{h_k}\hat{\boldsymbol{z}} \times (\boldsymbol{u}_k h_k) + \nabla\left(M_k + \frac{|\boldsymbol{u}_k|^2}{2}\right) = \delta_{1k}\frac{\boldsymbol{\tau}}{\rho_0 h_1} - \delta_{3k}\frac{C_d}{h_k}|\boldsymbol{u}_*|\boldsymbol{u}_k + \nabla\cdot\boldsymbol{\sigma}_k, \qquad (2.1a)$$

$$\frac{\partial h_k}{\partial t} + \nabla\cdot(\boldsymbol{u}_k h_k) = R_h(h_k). \qquad (2.1b)$$

where $\boldsymbol{u}_k$ is the horizontal velocity, $f = f_0 + \beta y$ is the planetary vorticity following the beta-plane approximation, $\zeta_k = \hat{\boldsymbol{z}}\cdot\nabla\times\boldsymbol{u}_k$ is the vertical component of relative vorticity, $\hat{\boldsymbol{z}}$ is the unit vector in the vertical direction, h_k is layer thickness, δ_{ij} is the Kronecker delta, ∇ is the horizontal (isopycnal) gradient, and M_k is the Montgomery potential. The wind stress $\boldsymbol{\tau}$ is steady, asymmetric, and non-zonal (figure 1a). The bottom stress is calculated from a linear drag law that depends on a prescribed near-bottom flow speed $|\boldsymbol{u}_*|$ and coefficient C_d. The horizontal and vertical stress tensor $\boldsymbol{\sigma}_k$ is parameterized by a Laplacian viscosity. A relaxation term $R_h(h_k) = \delta_{1k} r(h_r - h_k)$ is applied to the upper layer thickness to keep it close to a reference profile h_r at a rate of r. The relaxation is needed to maintain a sharp eastward extension of the boundary current. Detailed description of the terms in the equations is in Appendix A.

The square domain ($L_x \times L_y$ = 3840 km × 3840 km) is closed by solid boundaries, where free slip and no normal flux boundary conditions are applied. The equations are discretized on a uniform high-resolution (eddy-resolving) grid of 3.75 km resolution (1024^2 grid cells) with a time step of 50 s. We also use a coarse-resolution (non-eddy-resolving) grid of 60 km resolution (64^2 grid cells).

The model is spun up for 20 years from the state of rest to reach a statistically steady flow. It is then run for 4 additional years with all model fields saved every 6 hours as both the 6-hour averaged quantities and snapshots. Figures 1b-d show the ocean circulation in the eddy-resolving simulation. The model develops a strongly eddying double-gyre flow, separated by a meandering jet extending from the western boundary and representing the Gulf Stream or Kuroshio extension. It will be referred to as the Eastward Jet Extension (EJE) hereafter. A near-zonal front of potential vorticity (PV), characterized by large meridional PV gradients, is formed along the EJE (figure 1c).

2.2. *Tracer model*

The evolution of tracer concentration c in each layer is governed by

$$\frac{\partial(hc)}{\partial t} + \nabla\cdot(\boldsymbol{U}c) = \nabla\cdot(\kappa_{tr} h \nabla c) + R_{tr}(c) \qquad (2.2)$$

where $\boldsymbol{U} = \boldsymbol{u}h$ is the horizontal mass flux, $R_{tr}(c) = r_{tr} h(c_r - c)$ is relaxation of the tracer back to its initial distribution c_r, r_{tr} is the relaxation rate, and the layer subscript is omitted hereafter. The relaxation is applied in the upper layer only and is intended to mimic interactions with the atmosphere and prevent the tracer field from rapid homogenization. We set the subgrid tracer diffusivity $\kappa_{tr} = 100$ m^2 s^{-1} for all tracer simulations in this study. Tracers are initialized on the first day of year 21 and are simulated for 2 years.

We consider two idealized tracers with spatial distributions relevant to the real ocean properties. The tracers are initialized with a vertically and zonally uniform distribution. For the robustness of the conclusions, we chose tracers with very different initial meridional profiles. One tracer has an initial southward gradient (values increasing from north to south) generally consistent with the observed annual-mean sea surface temperature (SST), and a

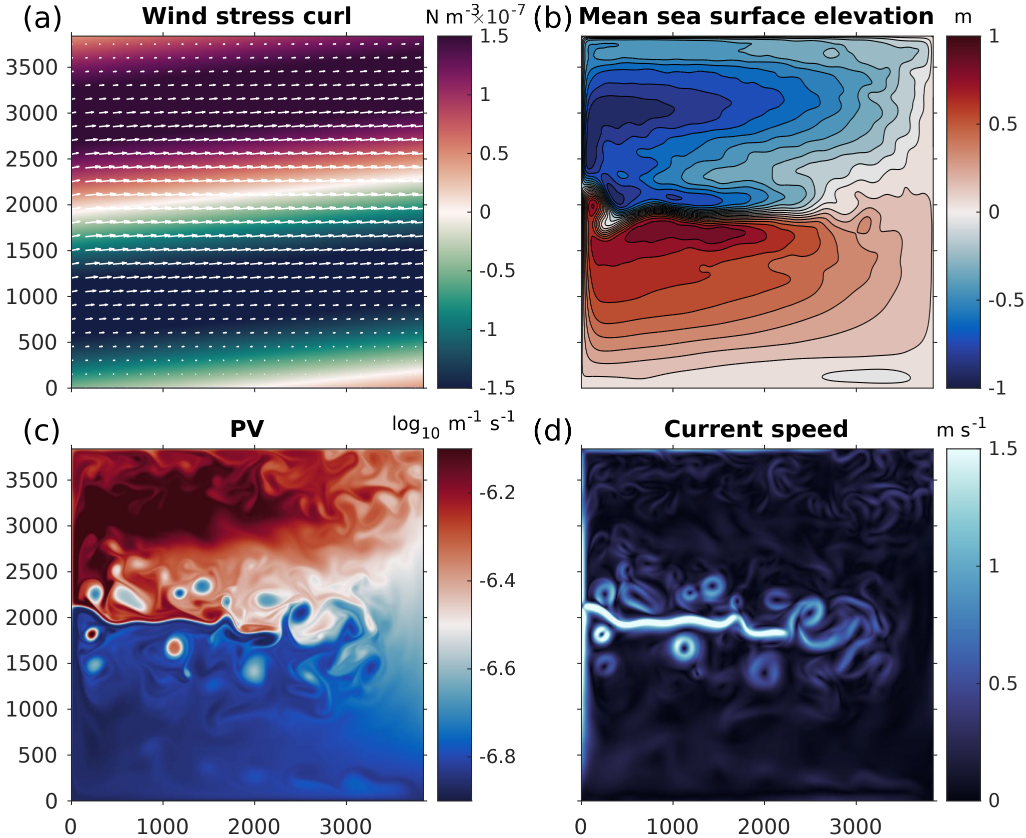

Figure 1: High-resolution simulations. (*a*) Wind stress vector and its curl. (*b*) Sea surface elevation averaged from year 21 to year 23. Snapshots of (*c*) potential vorticity and (*d*) current speed at day 120 year 21. All fields are shown in the upper layer.

relaxation time scale of $1/r_{tr} = 400$ d that mimics the dependence of the surface heat flux on SST (Haney 1971). We call it a "passive temperature" tracer. The other tracer has an initial northward gradient (values increasing south to north) that is typical of chemical tracers with higher solubility at cold temperatures such as CFC-11. It has a relaxation time scale of 125 d that mimics the time scale associated with the gas transfer of CFC-11 with the atmosphere (England *et al.* 1994). We call it a "chemical" tracer. Despite having initial profiles analogous to SST and CFC-11, these idealized tracers should not be interpreted as realistic simulations of these real-ocean properties. For additional analysis of the sensitivity of the results to tracers, we will also use eight additional color-dye tracers with initial linear and sinusoidal distributions (Appendix B).

Figure 2 shows the initial profiles and subsequent solutions in the high-resolution model. For the passive temperature, the western boundary currents bring warm (cold) water from subtropical (subpolar) gyre to the latitude of the EJE ($y \approx 2000$ km), where the warm and cold currents meet and continue eastward. The warm and cold waters retain their temperature contrast avoiding strong mixing with each other, indicating a presence of a partial mixing barrier along the EJE axis (Rypina *et al.* 2011, 2013; Kamenkovich *et al.* 2019). This confluence of cold and warm water creates a large negative meridional gradient (i.e. a sharp temperature front) along the jet extension. Similar features are observed for the chemical tracer, except that the front is characterized by large positive meridional gradient.

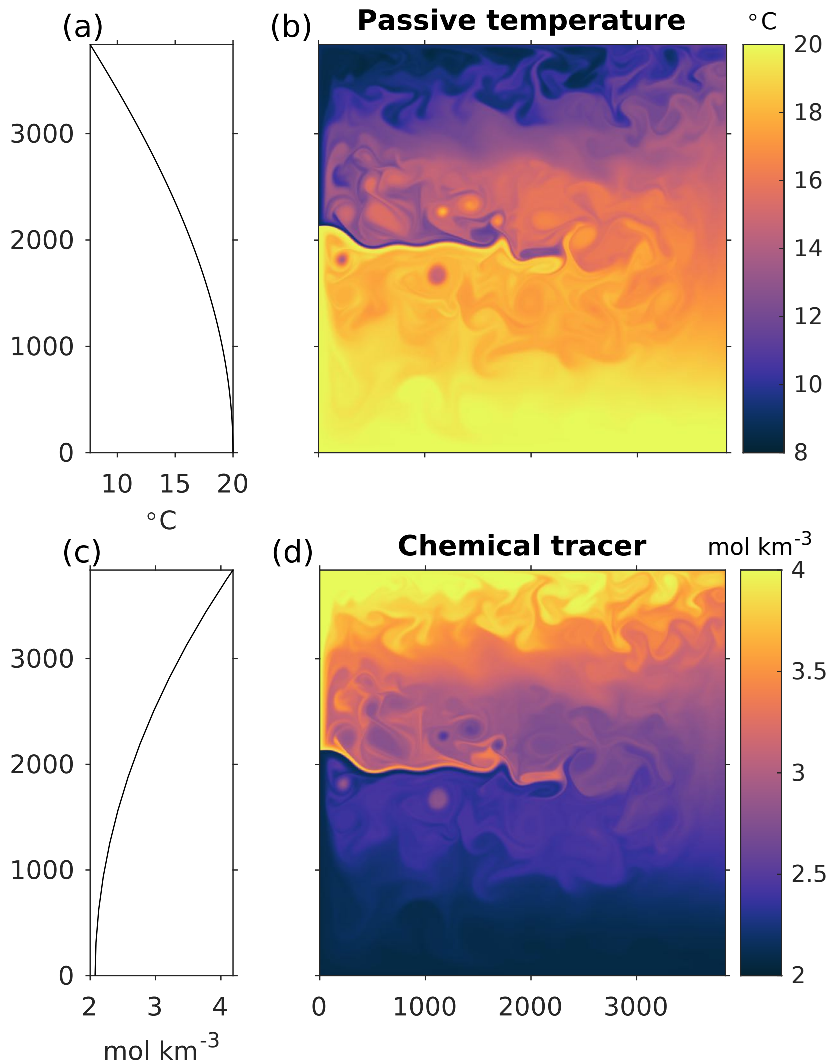

Figure 2: (a) Initial meridional profile and (b) upper layer tracer solution at day 120 year 21 for the passive temperature tracer. (c)-(d) Same but for the chemical tracer.

The focus of this study is on the effect of mesoscale eddies on a large-scale tracer front. For this purpose, we also perform tracer simulations on a coarse-resolution grid in which the eddies are not resolved:

$$\frac{\partial(h_L c_L)}{\partial t} + \nabla_c \cdot (\boldsymbol{U}_L c_L) = \nabla_c \cdot (\kappa_{tr} h_L \nabla c_L) + R_{tr}(c_L) + \mathcal{D} \tag{2.3}$$

where the subscript L denotes the large-scale fields on the coarse grid, ∇_c is a horizontal gradient on the coarse grid, and $\mathcal{D}$ is a term representing subgrid eddy effects.

Eddies can affect large-scale tracer concentration c_L through three pathways: (i) the dynamical modulation of the large-scale velocity $\boldsymbol{u}$ in (2.1a); (ii) the eddy-induced mass/density transport $\boldsymbol{U}_L - \boldsymbol{u}h_L$ and its effects on h_L in (2.1b) and c_L in (2.3); and (iii) the direct eddy tracer effect $\mathcal{D}$ to be discussed below. The coarse-grid solution c_L will be different from the fine-grid solution c from (2.2) unless all three effects are represented accurately.

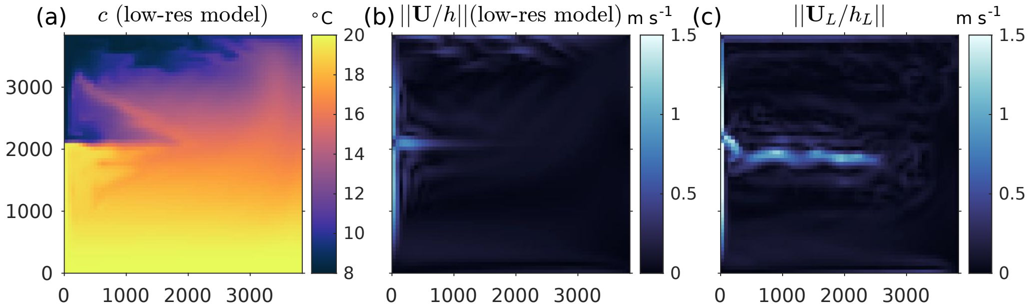

Figure 3: (a) The passive temperature tracer and (b) residual velocity speed (large scale plus GM velocities) simulated in the non-eddy-resolving model. (c) The residual velocity speed derived from the eddy-resolving model solution. Its derivation is given in section 3.1. All fields are diagnosed at day 120 year 21 in the upper layer. Note that in this study we mainly use (c).

Full coarse-grid simulations, that is, solutions of (2.1) and (2.2) on the coarse grid, predictably result in large biases in the position and intensity of the EJE and the associated tracer front. The biases manifest the importance of the dynamic and density effects of eddies (i)-(ii) that are missing in the coarse-grid simulations. Although these biases can potentially be alleviated by parameterizations of the momentum fluxes in (2.1a) and eddy-induced mass fluxes in (2.1b), e.g., by using the momentum eddy viscosity and the Gent-McWilliams (GM) closure (Gent *et al.* 1995), respectively, our attempt to use constant coefficients in both schemes failed to improve simulation of the front. Figures 3a-b show the passive temperature tracer and the residual velocity: the sum of the large-scale velocity solved by the model and the eddy-induced velocity parameterized by the GM scheme, in the coarse-grid simulation. A typical GM coefficient of 400 $\mathrm{m}^2\ \mathrm{s}^{-1}$ and a scale-selective Smagorinsky eddy viscosity (Smagorinsky 1963) with a nondimensional parameter of 0.15 are used. We see that the tracer front barely extends eastward and has a different position from the high-resolution front (figure 2b), which is mainly a result of a biased EJE (figure 3b).

In this study, we chose to focus on the direct stirring effect of eddies (term $\mathcal{D}$) and to derive $\boldsymbol{U}_L$ directly from the eddy-resolving solution instead of solving it in the non-eddy-resolving model. This approach ensures that the tracer on the coarse grid is advected by the "correct" residual flow $\boldsymbol{U}_L$, and we will demonstrate that it is not enough to represent a realistic tracer front. We employ the offline method that uses precalculated mass flux and layer thicknesses to solve the tracer equation (2.3). The method has been used for studies on the importance of mesoscale currents in tracer transports (Kamenkovich *et al.* 2017, 2021; Kamenkovich & Garraffo 2022) and the representation of eddy-induced advection and diffusion (Lu *et al.* 2022). Note that by using such an exact full mass flux, we do not need to include the GM closure, and our study is concerned with those eddy effects that even a "perfect" parameterization of the eddy mass fluxes cannot represent.

To ensure that there are no spurious sources of tracer mass, the large-scale layer thickness used in (2.3) is solved from the continuity on the coarse grid, with prescribed large-scale mass fluxes:

$$\frac{\partial h_L}{\partial t} + \nabla_c \cdot \boldsymbol{U}_L = R_h(h_L), \tag{2.4}$$

where the relaxation rate of layer thickness has the same value as the high-resolution model. The continuity and tracer time steps on coarse grid are 600 s.

We estimate the errors due to the offline calculations of tracer flux divergence, by comparing online and offline simulations of the passive temperature tracer. We confirmed that the errors are sufficiently small to warrant the use of the offline method for passive tracer simulations. The comparison is described in Appendix C.

3. Tracer eddy forcing and frontogenesis equation

In this section, we discuss a definition of the eddy forcing, derive the equation for the meridional tracer gradient that governs the evolution of the EJE front, and briefly discuss the generalized advective model for eddy effects on the tracer front.

3.1. *Tracer eddy forcing*

Mesoscale eddies lead to cross-scale transfer of energy and tracer (and its variance), so a non-eddy-resolving tracer model needs a subgrid tracer "forcing" to account for contributions of the unresolved scales to the large (resolved) scales. We define this tracer eddy forcing as the source term that augments the coarse-grid tracer solution towards a reference "truth", given a particular large-scale flow on the coarse grid (Berloff *et al.* 2021; Agarwal *et al.* 2021). In this study, we define the truth as the coarse-grained eddy-resolving tracer solution. Here, the coarse graining of a fine-grid solution is defined as spatial averaging over the coarse-grid cell of 60 by 60 km (16 by 16 fine grid points). The corresponding eddy forcing is obtained by coarse-graining the high-resolution tracer equation (2.2), subtracting the result from the coarse-grid equation (2.3), and requiring that $c_L = \langle c \rangle$ where angle bracket is the coarse-graining operator, which gives

$$\frac{\partial(h_L\langle c\rangle)}{\partial t} + \nabla_c \cdot (\boldsymbol{U}_L\langle c\rangle) = \nabla_c \cdot (\kappa_{tr} h_L \nabla\langle c\rangle) + R_{tr}(\langle c\rangle) + \mathcal{D}_e \tag{3.1}$$

Here, $\mathcal{D}_e$ is the tracer eddy forcing that can be diagnosed from the high-resolution model solutions, the given large-scale flow $\boldsymbol{U}_L$ and layer thickness h_L, and the coarse-grained tracer $\langle c\rangle$:

$$\begin{aligned}\mathcal{D}_e = {} & \frac{\partial(h_L\langle c\rangle)}{\partial t} - \frac{\partial\langle hc\rangle}{\partial t} + \nabla_c \cdot (\boldsymbol{U}_L\langle c\rangle) - \langle\nabla\cdot(\boldsymbol{U}c)\rangle \\ & + \langle\nabla\cdot(\kappa_{tr} h\nabla c)\rangle - \nabla_c\cdot(\kappa_{tr} h_L\nabla\langle c\rangle) + \langle R_{tr}(c)\rangle - R_{tr}(\langle c\rangle).\end{aligned} \tag{3.2}$$

At this point, the entire coarse-resolution system (eqs. 2.4, 3.1, and 3.2) hinges on the definition of the large-scale mass flux $\boldsymbol{U}_L$, which needs to be prescribed. We choose to define it as a coarse-grained and time-filtered high-resolution mass flux:

$$\boldsymbol{U}_L = \langle\overline{\boldsymbol{U}}\rangle \tag{3.3}$$

where the overbar is a 180-day sliding average, which, together with the coarsening removes the mesoscale variability. This is motivated by the fact that mesoscale eddies are often characterized by time scales of a few months. We also tested a 2-year time mean, and confirmed that it does not change our main conclusions in this study. To make sure that the divergence of $\boldsymbol{U}$ is preserved on the coarse grid, we decompose $\boldsymbol{U}$ into its divergent and rotational components and then coarse grain them separately. The derived $\boldsymbol{U}_L$ is shown in figure 3c. It retains the intensity and position of the EJE in the high-resolution model. Further details on its derivation are given in Appendix D.

The diagnosed eddy forcing $\mathcal{D}_e$ has complex spatial structure (figure 4a-c). Its high-magnitude values are concentrated along the EJE, where eddies cause significant redistributions of a large-scale tracer. The standard deviation exceeds the time-mean in most of the domain, indicating significant time variability in the eddy effects.

According to (2.3), (3.1) and (3.2), $\mathcal{D}_e$ should in theory be able to augment the coarse-grid

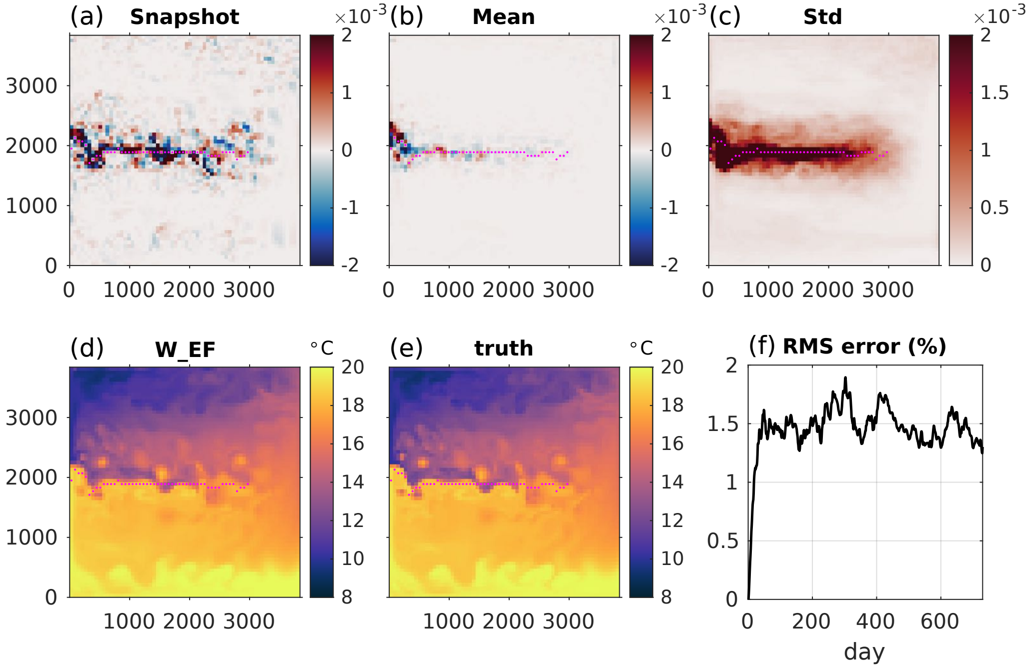

Figure 4: Eddy forcing for the passive temperature tracer and its skill of augmenting the coarse grained solution towards the truth. (*a*) Snapshot, (*b*) time-mean and (*c*) standard deviation over 2 years (years 21-22). Unit is [°C m s^{-1}]. (*d*) The passive temperature solved in the W_EF simulation. (*e*) The coarse-grained high-resolution solution ("truth"). (*f*) RMS value (multiplied by 100) of the relative error in the tracer in W_EF (relative to the truth) vs. time. Y-axis units are [%]. Snapshots are in the upper layer on day 361 year 21. Magenta dots are the EJE core defined by the maximal speed of the large-scale velocity $\boldsymbol{u}_L$ in the EJE region ($0 < x < 3000$ km, $1600 < y < 2400$ km).

model toward the true tracer concentration $\langle c \rangle$. To explore the extent to which it applies to our numerical application, we simulated the passive temperature tracer in a control experiment with $\mathcal{D} = \mathcal{D}_e$ (W_EF) in tracer equation (2.3). However, we found that after only about 10 days, the augmented solution significantly diverges from the truth. This is because $\mathcal{D}_e$ has a complex spatial pattern and temporal variability, and its augmenting efficiency depends critically on its spatial and temporal relation to the large-scale flow. Even small errors in this relation can quickly grow leading to large local biases in the solution. A similar issue was reported by Berloff *et al.* (2021) in their PV eddy forcing. To alleviate this deficiency, we ran the W_EF experiment with additional relaxation of the solution toward the truth, saved the relaxation forcing, and added it to the original $\mathcal{D}_e$ to get a new eddy forcing $\mathcal{D}_e^\dagger$. In this case, small differences due to the numerical errors are absorbed in $\mathcal{D}_e^\dagger$. The relaxation term is verified to be small compared to the original $\mathcal{D}_e$, but sufficient to suppress growing numerical errors. We confirmed that $\mathcal{D}_e^\dagger$ is statistically nearly identical to $\mathcal{D}_e$, and deviations due to the added relaxation forcing have an area r.m.s. value of about 6% of $\mathcal{D}_e$. We reran W_EF with the new forcing $\mathcal{D}_e^\dagger$ and no additional relaxation and confirmed that the solution indeed stays close to the truth with a relative difference of less than 2% (figure 4d-f). Henceforth, we will use the new eddy forcing for the following analysis, and we will omit superscript "†".

To demonstrate the importance of eddies in the large-scale tracer distribution, we run an experiment with $\mathcal{D} = 0$ (NO_EF). Figures 5a-b compare the passive temperature solutions in NO_EF and W_EF. The most important difference is in the vicinity of the front along

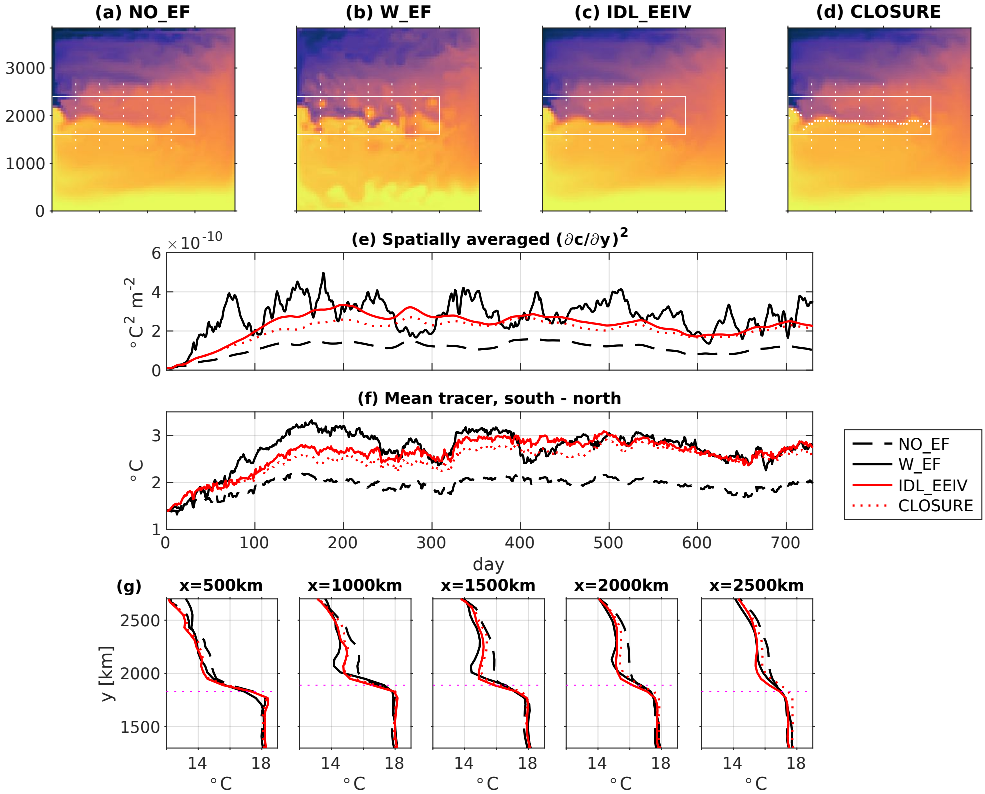

Figure 5: Passive temperature tracer solutions in the (*a*) NO_EF, (*b*) W_EF, (*c*) IDL_EEIV and (*d*) CLOSURE experiments on day 361 year 21. Unit is [°C]. Solid white lines show the boundaries of the EJE region in which the spatial average is performed. Zonal dots are the EJE core that divides the EJE region into the "north-of-jet" and "south-of-jet" region. Meridional dotted lines show the longitudes at which the profiles are diagnosed. Data are in the upper layer. (*e*) The squared meridional tracer gradient averaged along the EJE core. (*f*) The difference between the tracer inventory area-averaged in the south-of-jet and north-of-jet regions. (*g*) The meridional profiles of the 2-year (years 21-22) mean tracers in all the experiments.

the EJE. There is less warm (cold) water at the southern (northern) side of the EJE core in NO_EF, leading to a significantly weaker temperature front. We can quantify the strength of the front by three metrics: the squared meridional tracer gradient averaged along the EJE core (figure 5e), the tracer difference between the south and north of the EJE (figure 5f), and the meridional tracer profiles across the EJE (figure 5g). We see that the gradient on the EJE in W_EF is nearly twice as large as in NO_EF. The temperature difference in W_EF is about 1 degree (50%) larger than in NO_EF. The meridional profiles also show sharper tracer gradients in different positions of EJE in W_EF than NO_EF. These results demonstrate that the front is significantly weaker in the absence of eddy stirring, despite the correct large-scale advection $\boldsymbol{U}_L$ and eddy mass fluxes. This conclusion suggests that the stirring by mesoscale eddies significantly sharpens the front, which will be further confirmed in the following sections.

3.2. *Frontogenesis equation*

To explore the eddy-driven sharpening of the EJE front ("frontogenesis"), we derive the equation governing the evolution of a tracer gradient on coarse grid. We first combine the coarse-grid tracer equation (2.3) and continuity (2.4) to get the advective form of the tracer equation:

$$\frac{\partial c_L}{\partial t} + \boldsymbol{u}_L \cdot \nabla_c c_L = \frac{\mathcal{D}}{h_L} + \frac{\nabla_c \cdot (\kappa_{tr} h_L \nabla_c c_L)}{h_L} + \frac{R_{tr}(c_L) - c_L R_h(h_L)}{h_L} \tag{3.4}$$

where $\boldsymbol{u}_L = \boldsymbol{U}_L/h_L$ is the large-scale (residual) velocity that includes the effect of eddy-induced mass flux. Due to the beta-effect, tracer gradients along the near-zonal EJE front are nearly meridional, and we focus our analysis on the meridional direction. Applying $[(\partial_y c_L)\partial_y]$ to (3.4), we arrive at the equation of the (squared) meridional tracer gradient (a.k.a. frontogenesis equation; Mudrick 1974; Hoskins 1982; McWilliams 2021):

$$\frac{\partial}{\partial t}(\partial_y c_L)^2 = L + E + A + R, \tag{3.5}$$

$$\begin{aligned}
L &= -2(\partial_y c_L)\partial_y(\boldsymbol{u}_L \cdot \nabla_c c_L),\\
E &= 2(\partial_y c_L)\partial_y(\mathcal{D}/h_L),\\
A &= 2(\partial_y c_L)\partial_y(\nabla_c \cdot (\kappa_{tr} h_L \nabla_c c_L)/h_L),\\
R &= 2(\partial_y c_L)\partial_y((R_{tr}(c_L) - c_L R_h(h_L))/h_L).
\end{aligned}$$

Here L describes the effects of the large-scale advection which consist of two distinct mechanisms: (i) the large-scale advection of the squared tracer gradient $L_{adv} = -\boldsymbol{u}_L \cdot \nabla_c(\partial_y c_L)^2$ and (ii) the confluence of large-scale velocity $L_{con} = -2(\partial_y c_L)(\partial_y \boldsymbol{u}_L \cdot \nabla_c c_L)$, where $\partial_y \boldsymbol{u}_L$ is the meridional velocity gradient tensor. E is the eddy effect on the tracer gradient, and A and R represent the effects of subgrid diffusion and relaxations, respectively.

3.3. *The generalized advective–diffusive model*

For an approximation $\hat{\mathcal{D}}_e$ of the full eddy forcing $\mathcal{D}_e$, we use here a generalized advective–diffusive framework recently proposed by Lu *et al.* (2022):

$$\hat{\mathcal{D}}_e = \kappa h_L \nabla_c^2 c_L - \boldsymbol{\chi} \cdot h_L \nabla_c c_L, \tag{3.6}$$

where κ is an isotropic eddy diffusivity and $\boldsymbol{\chi}$ is an eddy-induced velocity (EIV). Lu *et al.* (2022) showed that this formulation can accurately reproduce the eddy-induced advection in a high-resolution model. Here, we use this approach to explore the advective effects of eddies on front evolution.

In frontal zones, the advective velocities $\boldsymbol{u}_L$ and $\boldsymbol{\chi}$ tend to be strong and nearly parallel to large-scale tracer contours whereas only their components that are perpendicular to the tracer contours are significant for tracer distribution. We, therefore, introduce here "effective eddy-induced velocity" or EEIV. EEIV is conceptually analogous to the "effective diffusivity" (e.g. Nakamura 1996) since it is also applied on the direction perpendicular to the tracer contours. We will later demonstrate that this scalar formulation has several advantages over using the vector $\boldsymbol{\chi}$. We will later also use a similarly defined effective large-scale velocity (ELSV).

Equation (3.6) then becomes

$$\hat{\mathcal{D}}_e(\kappa, \chi_\perp; c_L) = \kappa h_L \nabla_c^2 c_L - \chi_\perp |h_L \nabla_c c_L| \delta_c, \tag{3.7}$$

where the EEIV $\chi_\perp = \boldsymbol{\chi} \cdot \boldsymbol{n} \delta_c$, $\boldsymbol{n}$ is the unit vector along tracer gradient $\boldsymbol{n} = h_L \nabla_c c_L / |h_L \nabla_c c_L|$, and δ_c is a sign function depending on the direction of the zonal-

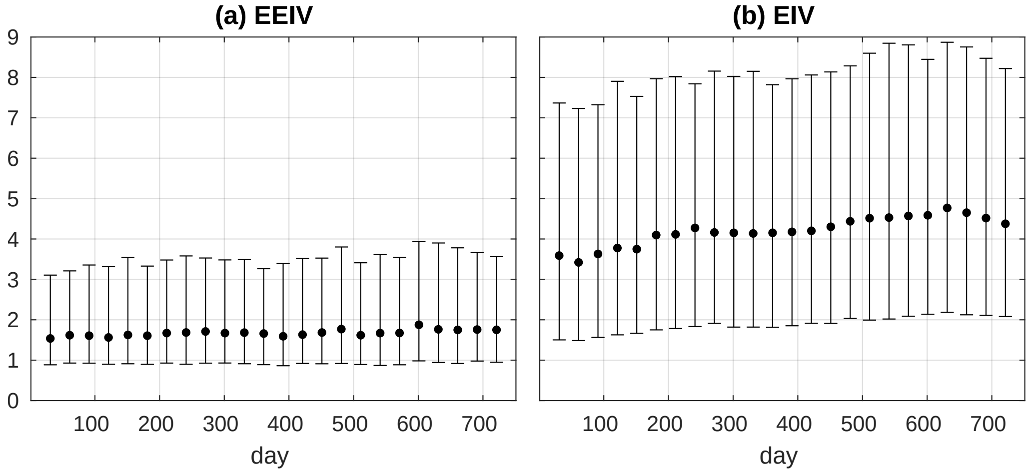

Figure 6: Tracer dependence, calculated as a ratio of the standard deviation to the absolute ensemble mean, of (a) EEIV $\chi_\perp$ and (b) EIV $\boldsymbol{\chi}$. Error bars denote the median and the 25–75th percentile range of the ratio. The ensemble of EEIV includes 10 estimates diagnosed from 10 (passive temperature tracer, chemical tracer and eight idealized tracers) tracers. The ensemble of EIV includes 10 estimates randomly chosen from all the 45 estimates (45 tracer pairs generated from 10 tracers). For EIV, the ratios of its two horizontal components are averaged. Data are in the upper layer.

mean meridional tracer gradient:

$$\delta_c = \begin{cases} 1, & \overline{h_L \partial_y c_L}^x > 0 \\ -1, & \overline{h_L \partial_y c_L}^x < 0. \end{cases} \tag{3.8}$$

The function is introduced to simplify interpretation of the scalar $\chi_\perp$ and eliminates its dependence on the direction of the large-scale tracer gradient. For example, a northward EIV $\boldsymbol{\chi}$ has a positive projection ($\boldsymbol{\chi} \cdot \boldsymbol{n} > 0$) onto a front with northward tracer gradient ($\delta_c = 1$) but has a negative one onto a front with southward gradient ($\delta_c = -1$). By multiplying by δ_c, $\chi_\perp$ becomes positive in both cases and can be interpreted as speed at which eddies displace tracer contours.

Note that using the advective approach has clear advantages in this study focused on eddy-driven frontogenesis, since this is a fundamentally non-diffusive process (McWilliams 2021). Although, technically speaking, gradient sharpening can be achieved by negative diffusivity, its practical implementation causes numerical instability in models (Trias *et al.* 2020; Kamenkovich *et al.* 2021; Lu *et al.* 2022). Diffusive effects of eddies expressed via κ, however, can be important in the oceanic interior. Therefore, we set the eddy diffusivity κ as a positive constant $\kappa = 400\ \mathrm{m^2\ s^{-1}}$, which is an estimate of the domain-mean κ in the upper layer. The unknown, $\chi_\perp$, is calculated by inverting (3.7) with the diagnosed $\mathcal{D}_e$ on the left-hand side and c_L being the tracer solution of the W_EF simulation. For comparison, the vector EIV $\boldsymbol{\chi}$ is also calculated by inverting (3.6) using two tracers (two equations). More details of the inversion can be found in Haigh *et al.* (2020) and Lu *et al.* (2022).

One of the advantages of the scalar formulation (3.7) over the vector formulation (3.6) is the reduction of tracer dependence. The tracer dependence refers to the sensitivity of EEIV $\chi_\perp$ or EIV $\boldsymbol{\chi}$ to the initial tracer distributions and was reported for eddy diffusivity and eddy transport tensor (Bachman *et al.* 2015; Haigh *et al.* 2020; Kamenkovich *et al.* 2021; Sun *et al.* 2021; Lu *et al.* 2022). In theory, the eddy diffusivity and the (E)EIV are assumed to be quantities inherent to the eddy flow and independent of the tracer itself. The tracer dependence, therefore, contradicts this fundamental assumption and implies potential bias in representing eddy effects using these quantities. For example, Lu *et al.* (2022) showed that χ is less tracer dependent than the eddy diffusivity, which is interpreted as advantage of the advective formulation. Here we calculate the tracer dependence in the same way as Lu *et al.* (2022). We first calculate an ensemble of $\chi_\perp$ (χ) from a set of tracers (tracer pairs). The tracer dependence is then defined as the ratio of the ensemble standard deviation to the absolute ensemble mean of $\chi_\perp$ (χ). Figure 6 compares the ratios for $\chi_\perp$ and χ. We see that the tracer dependence of $\chi_\perp$ is significantly reduced compared to that of χ. Our additional analysis further shows that the sign function δ_c (3.8) is important for the reduction in tracer sensitivity. These results demonstrate the benefit of using the EEIV to represent the eddy effects.

The conservation of global tracer inventory when applying the EEIV formulation (3.7) is enforced using the method in Lu *et al.* (2022). A correction is added to the parameterized eddy forcing $\hat{\mathcal{D}}_e$, that makes its global integral zero in the closed domain. The correction is conceptually similar to the conservation enforcement widely used in stochastic parameterizations (Leutbecher 2017). We describe it and confirm the conservation in Appendix E.

4. Effect of eddies on the front

In this section, we explore the role of eddies in the frontal evolution by analyzing the tracer distribution and the frontogenesis equation in our numerical experiments. We only show the results for the passive temperature tracer but confirm that all conclusions remain the same for the chemical tracer as well.

4.1. *Analysis of the frontogenesis equation*

To examine how eddies interact with large-scale flow in sharpening the front, we study the frontogenesis equation (3.5) for the W_EF experiment. Figure 7a shows the time series of all terms in the budget averaged within the EJE region. The tendency term fluctuates around zero after the tracer is stirred up, showing that a statistically steady state of tracer is reached. Several important points are drawn from the budget. Firstly, the area-mean eddy term E remains positive, meaning that it acts to increase the magnitude of tracer gradients. This implies that eddies are sharpening the front, which agrees with the previous comparison between the NO_EF and W_EF simulations. In contrast, the effect of large-scale current, characterized by the negative L term of similar magnitude with E, is to weaken the front. There is also a large inverse spatial correlation of -0.9 between L and E, meaning that the large-scale and eddies are acting to balance each other in the front evolution. The residual (sum) of the two is at least one order of magnitude smaller than any of the terms and is balanced by the sum of the (squared) tracer gradient tendency, the diffusion A and the relaxation R. The diffusion remains negative and acts to reduce the magnitude of the front as anticipated. The relaxation has a very small magnitude and helps sustain the front. Figure 7b further shows the two components of L, both representing effects of the large-scale advection. The large-scale velocity confluence term L_{con} plays a dominant role in the weakening of the front, while the advection term L_{adv} occasionally counteracts L_{con} with a much smaller magnitude. The small magnitude of L_{adv} could be explained by the fact that the large-scale flow $\boldsymbol{u}_L$ in EJE is nearly perpendicular to the gradient of the squared tracer gradient.

To further explore the relationship between large-scale and eddy effects on the front, we compute the point-wise time correlations between the frontogenetic budget terms (figure 8). We see that large negative correlations between L and E are concentrated along the EJE, indicating strong mutual compensation between the large- and mesoscale processes in

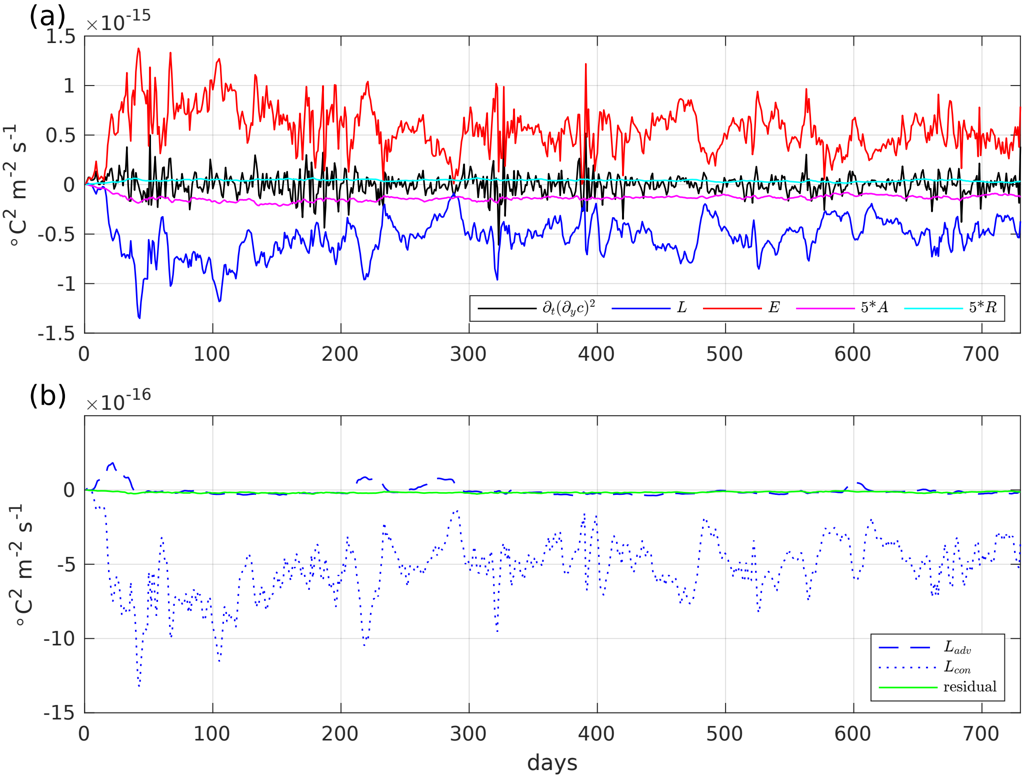

Figure 7: Time series of terms in the frontogenesis equation averaged in the EJE region (defined in Figure 5). (*a*) The tendency, L, E, A and R (A and R are multiplied by a factor of 5) terms. (*b*) The two components of L: L_{adv} and L_{con}, and the residual of the budget. Results are for the passive temperature tracer in the upper layer.

the region, where the eddy forcing is also particularly large (figure 4a-b). This correlation suggests a possibility of a potential closure for the EEIV $\chi_\perp$ in terms of the large-scale fields, that will be discussed in the next section. The tendency term in the jet region is not significantly correlated to either L or E alone, because the gradient is governed by the joint effect of large-scale and eddies, as indicated by the area-mean budget (time series). Outside of the jet region, the tendency is stronger correlated to E than L, which is likely due to the transient eddy effect on tracer contours. However, since the tracer concentrations there are not significantly different between the NO_EF and W_EF simulations and that our main focus is on the frontal region, we do not discuss the effect of eddies outside of the jet region. We also see that E is mainly negatively correlated with L_{con} rather than L_{adv} along the jet, re-confirming the dominant role of L_{con} in the large-scale flow effect.

4.2. *Importance of the eddy-induced advection*

Our results have so far demonstrated that mesoscale eddies sharpen the front while the large-scale flow plays an opposite role. We next use the concept of eddy-induced advection to demonstrate the compensation between eddies and large-scale currents. Note that the same analysis would be significantly less straightforward if the diffusivity tensor with negative diffusivities were used, because perfect compensation between advection and diffusion cannot be achieved for an arbitrary tracer. Figure 9 shows the standard deviation, time-mean and zonal-mean of the EEIV $\chi_\perp$, as well as the effective large-scale velocity (ELSV) $u_\perp = \boldsymbol{u} \cdot \boldsymbol{n}\delta_c$

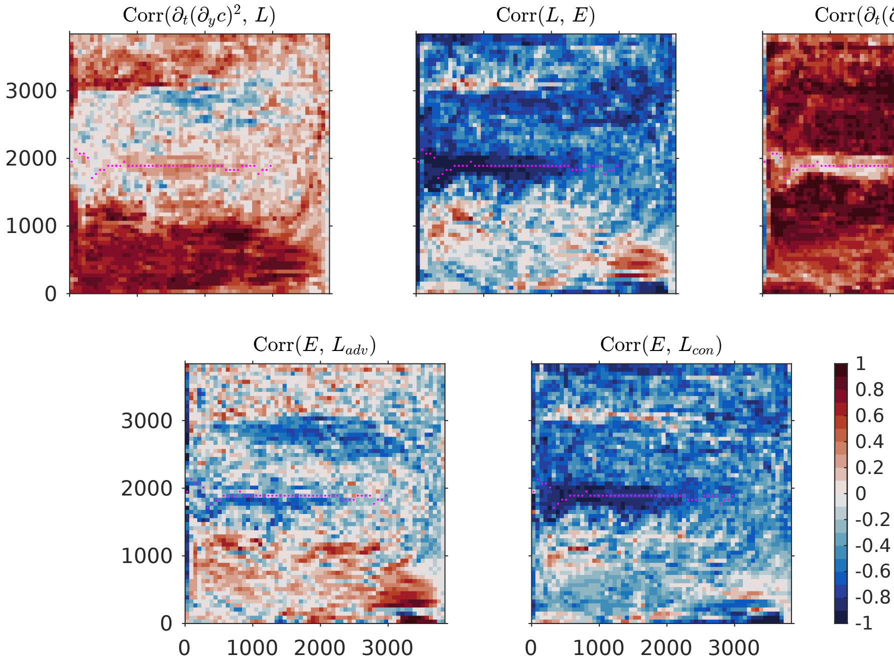

Figure 8: Pointwise time correlations between different terms in the frontogenesis equation over 2 years in the upper layer. Magenta dots are the EJE core.

for the passive temperature tracer. In general, $\chi_\perp$ and $u_\perp$ have the same order of magnitude, showing their equally important roles in tracer distributions. The std of $\chi_\perp$ exceeds its time mean and concentrates along the jet, indicating a large time variability as the eddy forcing. The time-mean $\chi_\perp$ is mostly negative (positive) at the north (south) of the core, which cools (warms) the cold (warm) water by imposing negative (positive) eddy forcing (figure 9b-c). The total effect is to amplify the negative gradient and sharpen the temperature front. The sign of $\chi_\perp$ also indicates that the EIV $\boldsymbol{\chi}$ across tracer contours at the north (south) of the EJE core is directed mainly southward (northward). That is, physically, the EIVs on both sides of the EJE squeeze the temperature contours together by bringing cold and warm water towards each other, thus sharpening the front. The eddy-induced squeezing of tracer contours has been reported by many studies in terms of up-gradient eddy-induced diffusion (Kamenkovich *et al.* 2021; Haigh *et al.* 2021*a*; Haigh & Berloff 2021). Here, it is effectively quantified by the eddy-induced advection. The ELSV $u_\perp$ has an opposite profile to $\chi_\perp$ in the EJE region (figure 9f), confirming the compensation between the two as discussed above.

5. Simulation of the front in coarse-resolution tracer model

The goal of this section is to explore parameterization of the tracer eddy forcing $\mathcal{D}_e$ using the EEIV $\chi_\perp$, i.e., let $\mathcal{D} = \hat{\mathcal{D}}_e(\chi_\perp; c_L)$ in (2.3). We will evaluate the skill of the EEIV $\chi_\perp$ in simulating the eddy-driven sharpening of the front and will propose a simple closure for its parameterization.

5.1. *Loss of skill for exact parameters*

Our first step toward parameterization is to apply the exactly fitted EEIV $\chi_\perp$ in the tracer simulation, using the tracer concentrations c_L taken from the W_EF simulation. We denote this experiment as EXACT_EEIV. The exact $\chi_\perp$ is calculated by inverting (3.7) for the passive

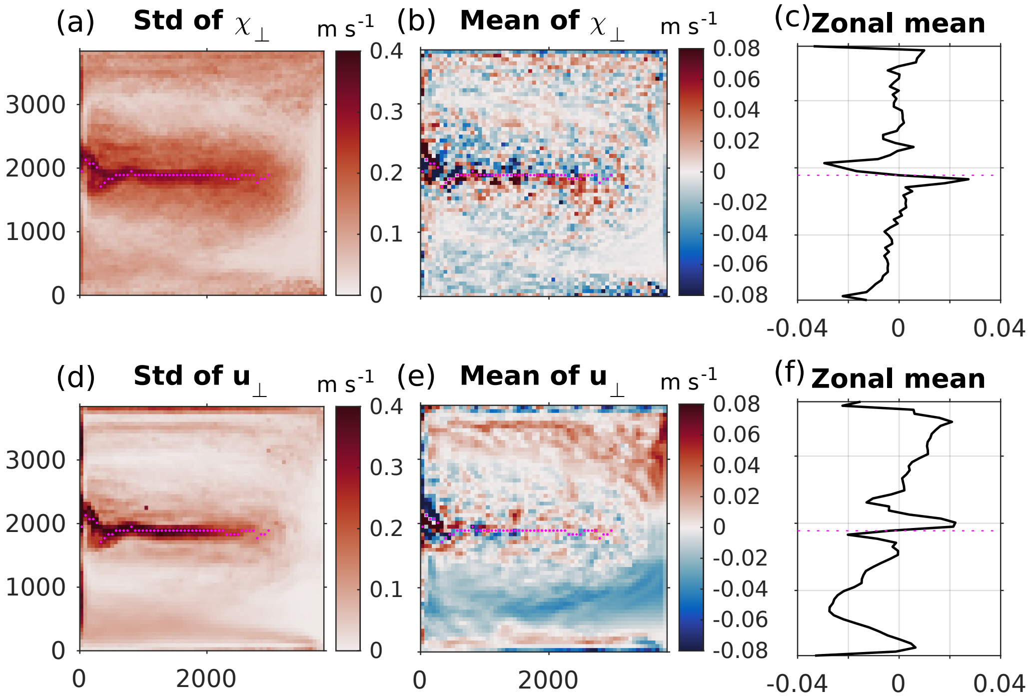

Figure 9: (a) The standard deviation, (b) time mean and (c) time- & zonal-mean of the EEIV $\chi_\perp$. (d)-(f) Same but for ELSV $u_\perp$. Both are projected onto the passive temperature tracer. The data is over year 21-22. Magenta dots in color plots are the EJE core. Magenta dotted line in (c) and (f) shows the zonal-mean latitude of the EJE core. Outliers in $\chi_\perp$ that fall below 1% percentile or above 99% percentile are excluded for presentation purposes.

temperature tracer. It should, in theory, be able to accurately reproduce $\mathcal{D}_e$ and the tracer concentration in W_EF. We, however, found large biases in the resulting solution. Figures 10a-c show the temperature solution in the EXACT_EEIV and time series of the meridional gradients defined in figure 5. Compared to W_EF (figure 5), the tracer has a large bias near the EJE core. Interestingly, the front becomes even weaker than in the NO_EF simulation, as evidenced by the tracer gradients (figures 10b-c to figures 5e-f). This shows a loss of skill of the exact $\chi_\perp$ in the jet extension region. In the rest of the domain the solution in EXACT_EEIV is visually indistinguishable from W_EF. However, the eddies there have relatively small effects on the large-scale tracer distribution, and our goal is not to reproduce individual features in the interior of the subtropical gyre.

The fact that the exact $\chi_\perp$ fails to reproduce a correct EJE front is likely due to the deterioration of the spatiotemporal co-variability of the front position and eddy forcing. The tracer front constantly changes its position due to the large-scale-eddy interaction, and the corresponding eddy forcing $\mathcal{D}_e$ and $\chi_\perp$ both have complex spatiotemporal dependence (figure 4a-c; figure 9a-b) that is closely related to the frontal evolution. Thus, to accurately reproduce the front, the parameterized eddy forcing $\hat{\mathcal{D}}_e(\chi_\perp; c_L)$ should capture this coupling with the front in both space and time. This is clearly a hard task because even a small error in the runtime solution c_L can cause an error in the eddy forcing $\hat{\mathcal{D}}_e$, and induce an error in the coupling between the front and $\hat{\mathcal{D}}_e$. The errors in the forcing can grow very fast due to chaotic sensitivity. For example, a bias in the eddy forcing can cause cooling in places where warming is needed for sharpening the front, which in turn amplifies errors in the solution.

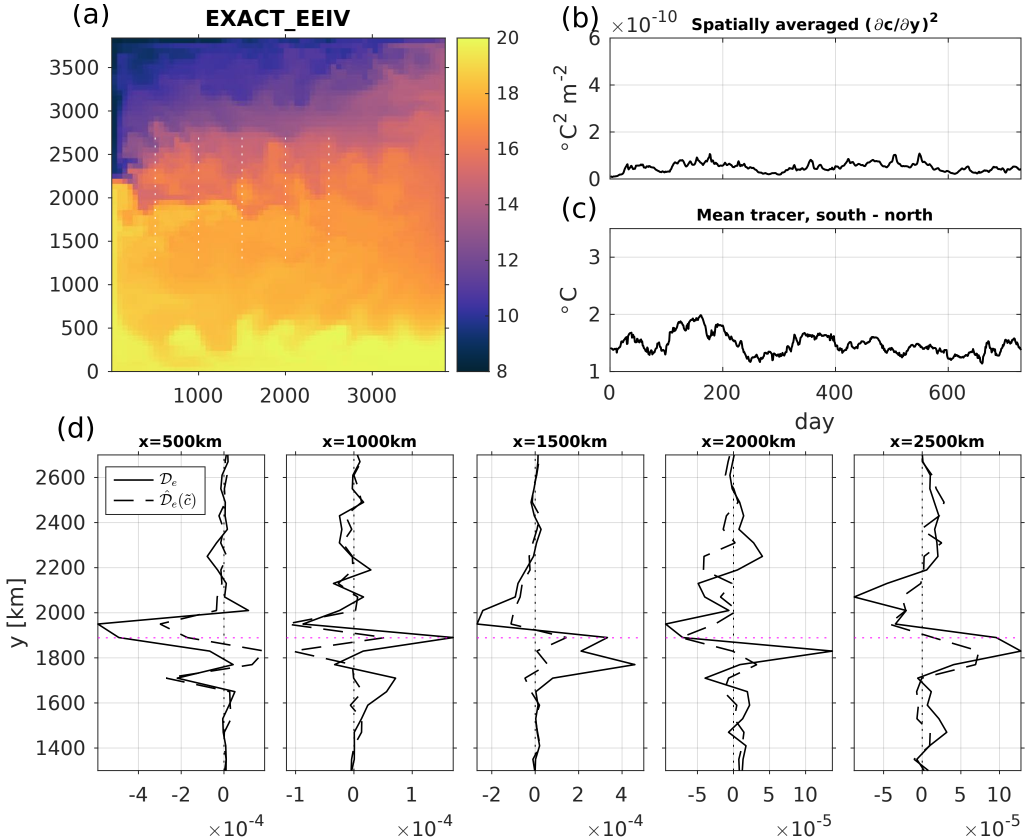

Figure 10: Passive temperature solution ([°C]) in the EXACT_EEIV simulation. (*a*) Snapshot at day 361 year 21. (*b*)-(*c*) The spatial averaged squared meridional tracer gradient and the tracer difference between the south and north of the EJE, respectively, as functions of time (same as in figures 5e-f). (*d*) Meridional profiles of the true eddy forcing $\mathcal{D}_e$ and the parameterized eddy forcing $\hat{\mathcal{D}}_e(\chi_\perp; c_L)$ diagnosed in the EXACT_EEIV run, at different longitudes shown by the white dots in (*a*). Magenta dots denote the latitudes of the EJE core.

Figure 10d compares several meridional sections of time averaged $\hat{\mathcal{D}}_e(\chi_\perp; c_L)$ and original full $\mathcal{D}_e$. We see that $\hat{\mathcal{D}}_e$ is generally much smaller than $\mathcal{D}_e$ around the front (1600 km $< y <$ 2400 km), and thus produces a much weaker front despite having "perfect" $\chi_\perp$. The eddy forcing is close to zero in the rest of the domain, where eddy activities are weak, showing that the tracer bias is concentrated in the front region of strong eddy effects. In the following section, we will see that an idealized, time-independent profile for $\chi_\perp$ will be more efficient in representing effects of eddies on the front.

5.2. *A simplified EEIV and its performance in simulations*

In the previous section, we observed that time varying, two-dimensional EEIV $\chi_\perp$ aggravates biases in the simulation, and suspect that this complexity is the cause of the problem. Small errors in tracer distribution can lead to positive feedback and further error amplification. This can happen if an important correlation between two complex fields, $\chi_\perp$ and c_L, is broken. To evaluate this hypothesis, we consider here a highly idealized $\chi_\perp$ profile designed to guarantee the eddy-driven frontogenesis. If successful, this simple model can pave way to parameterization of the process. The most straightforward choice is a time-independent and

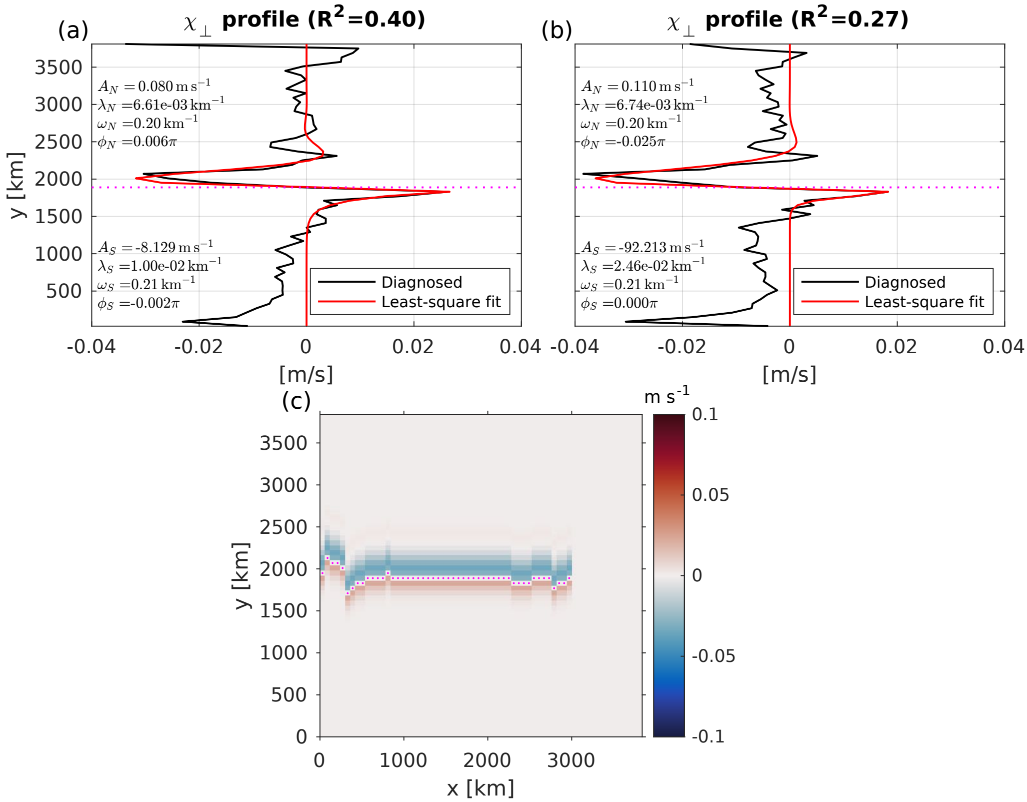

Figure 11: Meridional profiles fitted from the time- and zonal-mean EEIV $\chi_\perp$ diagnosed from the (*a*) passive temperature and (*b*) chemical tracers. The time mean is calculated over 2 years. (*c*) 2D $\chi_\perp$ field generated from the fitted profiles in (*a*) and (*b*). Magenta dots are EJE core.

zonally uniform profile. We have seen in figure 9b-c that $\chi_\perp$ is zero at the EJE core, rapidly grows to a large negative (positive) value in the north (south) and then decays away from the core. We fit this time- and zonal-mean profile of $\chi_\perp$ in a least-square sense by a simple damped sinusoidal function:

$$\hat{\chi}_\perp(y) = \begin{cases} A_N e^{-\lambda_N (y-y_{GS})} \sin(\omega_N (y - y_{GS}) + \phi_N), & y > y_{GS} \\ A_S e^{-\lambda_S (y_{GS}-y)} \sin(\omega_S (y_{GS} - y) + \phi_S), & y < y_{GS}, \end{cases} \tag{5.1}$$

where y_{GS} is the latitude of the jet core, subscripts N and S denote the parameters of the sinusoidal function in the north and south of the core, respectively. The $\chi_\perp$ profiles and fitted functions $\hat{\chi}_\perp(y)$ for the passive temperature and chemical tracers are shown in figures 11a-b. The two tracers, although having very different initial meridional distributions, give similar profiles of $\chi_\perp$. This is another manifestation of a modest tracer dependence in EEIV, as discussed in section 3. We then calculate an idealized 2D $\chi_\perp$ field from the fitted profiles as follows. At each longitude, $\chi_\perp$ is given by $\hat{\chi}_\perp(y)$ with y_{GS} being the latitude of the jet core at that longitude. The resulting $\chi_\perp$ fields from the two tracers are then averaged to generate the desired idealized $\chi_\perp$ field, as shown in figure 11c.

We next use the derived idealized field of the EEIV to simulate the passive temperature and chemical tracers on the coarse grid. We denote these experiments as IDL_EEIV. The strength of the front is measured here by the difference of the spatially averaged tracers on

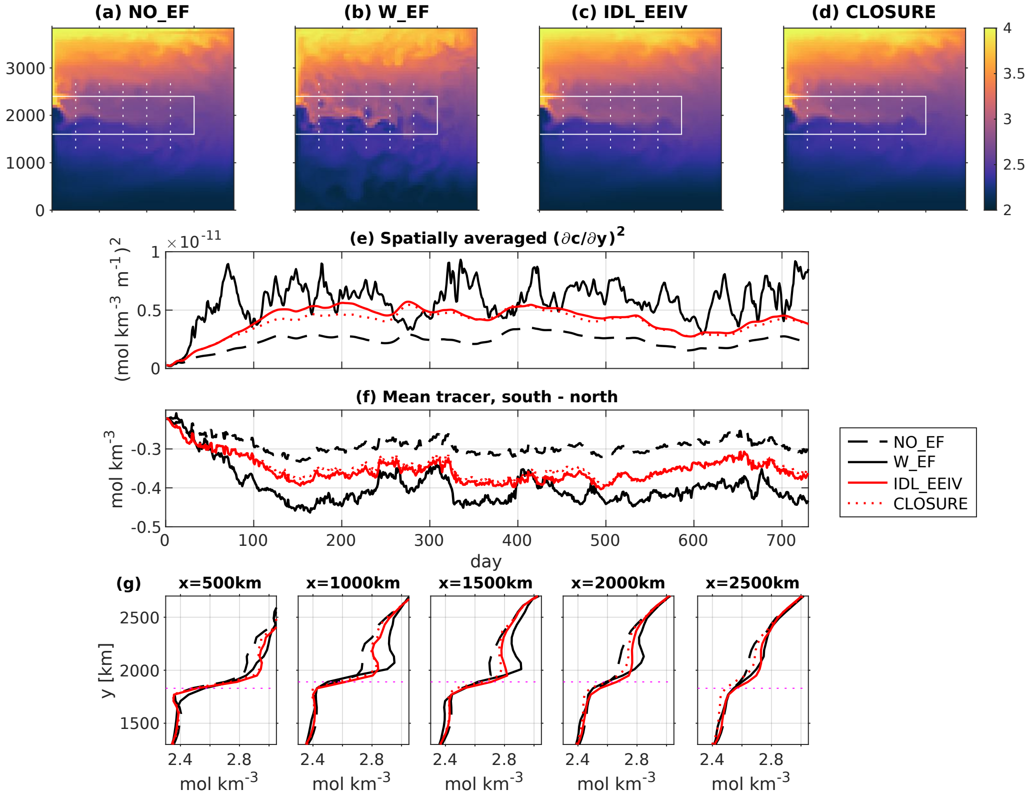

Figure 12: Same as Figure 5 but for the chemical tracer.

the two sides of EJE. Figure 5 shows the passive temperature solution and its gradient from the IDL_EEIV experiment in comparison to those from NO_EF and W_EF. We now see that the strong temperature gradients along the EJE and in the surrounding area are reproduced well by the idealized $\chi_\perp$ after the first 200 days (figure 5e-f). The meridional profiles further show that the meridional gradients across the EJE (figure 5g) improve relative to the NO_EF values, despite a small remaining bias in the position of the front, possibly caused by time dependence in the EJE position. The improvement in the simulation of the temperature front over the NO_EF case is expected since the forcing is designed to bring warm (cold) water to the south (north) of the EJE. This result is a clear demonstration of the advantage of using eddy advection over the eddy diffusion and an idealized EEIV profile over the 2D time-dependent EEIV, in representing the eddy-driven sharpening of front. The sharpening is relatively straightforward to enforce in our $\chi_\perp$ formulation, whereas it cannot be guaranteed by the vector χ, which is nearly parallel to the tracer contour, and, of course, cannot be achieved by positive diffusion.

Simulations of the chemical tracer with the same $\chi_\perp$ give similar results (figure 12), demonstrating a robustness of the formulation. The southward meridional tracer gradient in W_EF is 30% larger than in NO_EF, and our idealized $\chi_\perp$ can increase the magnitude of the gradient in NO_EF by about 15% (figure 12f). The slightly reduced skill in this case compared to the temperature simulation is due to the tracer dependence: the $\chi_\perp$ diagnosed from the chemical tracer is slightly larger than the one from the temperature tracer in the north of the EJE (figure 11a-b). As a result, it leads to a weaker eddy forcing.

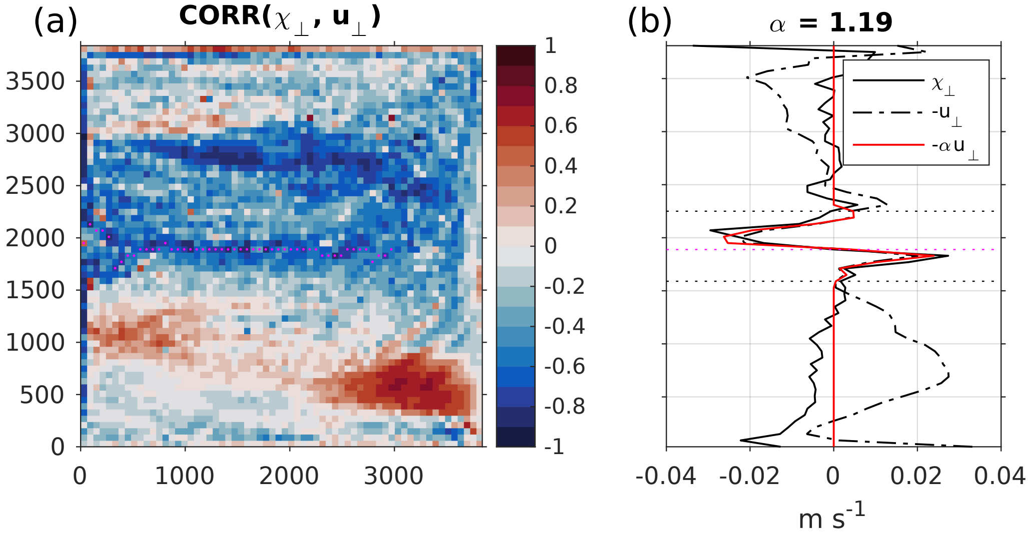

Figure 13: (a) Correlation between $\chi_\perp$ and $u_\perp$ over 2 years in the upper layer. (b) Meridional profiles of the time- and zonal- mean $\chi_\perp$ (black solid) and minus $u_\perp$ (dot dash). Horizontal black dots show latitudes of the data from which α is estimated. Magenta dots are the EJE core. Red solid line is the predicted $\chi_\perp$ by the fitted α and $u_\perp$ profile.

5.3. *Closure of EEIV by the large-scale flow*

As the last step, we propose a closure for EEIV $\chi_\perp$ in terms of large-scale fields on the coarse grid. We have seen that the time- and zonal-averaged $\chi_\perp$ and ELSV $u_\perp$ have similar but opposing profiles within the latitudes of EJE (figures 9c,f). Figure 13a further shows significant negative correlation between the two fields around the jet; some positive values are, however, visible in the southern domain where the tracer is nearly uniform and is of little interest. This is also consistent with the correlation between the large-scale and eddy terms in the frontogenesis equation (figure 8). These results suggests a possibility that $\chi_\perp$ can be expressed linearly by $u_\perp$

$$\chi_\perp = -\alpha u_\perp, \tag{5.2}$$

where the coefficient α quantifies the balance between the two.

We next implement this closure in the tracer model by substituting it for $\chi_\perp$ in (3.7). To reduce the errors that could be caused by the variability in $\chi_\perp$ as discussed above, we ignore the temporal and zonal variability in $\chi_\perp$ and choose to predict an 1D profile:

$$\chi_\perp(y) = -\alpha \overline{u}_\perp^{xt}(y), \tag{5.3}$$

where $\overline{u}_\perp^{xt}(y)$ is the zonal and 2-year time mean ELSV. The predicted $\chi_\perp(y)$ will be extended to 2D by mapping at each longitude as previously done. The resulting 2D field will be applied to the model. Since the significant correlation between $\chi_\perp$ and $u_\perp$ is concentrated in the EJE region, we estimate α by minimizing the RMS error between the two profiles in the latitudes of EJE. The parameterized $\chi_\perp$ is shown in figure 13b. The coefficient α has a value of about 1.2, indicating a dominating role of eddy-induced advection in balancing the large-scale advection. Note that the value is different from unity, meaning the compensation between EEIV and ELSV is not complete. Also note that this α quantifies the time- and zonal mean relation between the two, and the instantaneous relation can be different. In fact, a pointwise regression of $\chi_\perp$ on $u_\perp$ resulted in a space-dependent coefficient (not shown) that ranges from -1 to -0.4 in the EJE region, indicating a partial balance in most places.

For practical applications, the coefficient α is not known a priori and has to be chosen as part of model "tuning". For example, our attempt to implement the above closure showed that the empirical value of 1.2 is not sufficient to reproduce a sharp front. We then tested a set of α and found that the magnitude of the front increases with larger α. This is expected because α controls the magnitude of the EEIV and tracer eddy forcing (3.7), thus affecting the front sharpness. This closure is similar to the amplification of the eddy backscatter proposed by Berloff (2018), which aims to parameterize the dynamic eddy effects on the EJE, whereas our closure aims at the eddy effects on tracer front.

Here we report the result of the test with $\alpha = 2$ (denoted as "CLOSURE") for the passive temperature and chemical tracers in figure 5 and 12, respectively. The closure reproduces a sharp front for both tracers as effectively as the IDL_EEIV simulation, indicating that it could be a promising parameterization of the eddy-driven frontogenesis. Note that the value of α possibly depends on the flow properties, e.g. the interaction between large-scale and eddies in front evolution, and thus needs to be carefully selected in different models and/or flow regimes.

6. Conclusions and discussion

This study investigates the importance of mesoscale eddies in the formation and evolution of large-scale oceanic tracer fronts along the eastward jet extension (EJE) of western boundary currents. Using an idealized eddy-resolving model of the double gyre system, we quantify the effects of eddies using the tracer "eddy forcing" on the coarse-resolution grid. As discussed by several previous studies, this approach has advantages over methods based on eddy fluxes, both because it incorporates all eddy terms in the tracer budget and because it avoids ambiguity associated with large non-divergent ("rotational") fluxes (Haigh *et al.* 2020; Kamenkovich *et al.* 2021; Lu *et al.* 2022). If the eddy forcing is simulated correctly in the coarse-resolution simulations, one can hope that the tracer field can be simulated accurately as well. This study focuses on the eddy-induced stirring of tracers, whereas the contribution of eddies to momentum and mass/density fluxes are outside its scope.

The key result is that mesoscale eddies sharpen the large-scale tracer front, as demonstrated by both the sensitivity tracer experiments in an offline model and the frontogenesis equation. This is manifested by a significantly sharper front in the simulation with the eddy forcing than in the run without, despite the mass fluxes being the same in both simulations. The analysis of the terms in the frontogenesis equation confirms this conclusion, and further shows that the large-scale current counteracts the eddy-driven frontogenesis, nearly compensating it in a steady state. The confluence (strain) of the large-scale velocity, rather than the large-scale advection of tracer gradients, plays a major role in the latter effect.

The frontal sharpening by eddies and mutual compensation of eddy-driven and large-scale advections in the frontogenesis can be conveniently quantified using a recently proposed generalized advective framework (Lu *et al.* 2022). In this study, we further modify this approach by using an effective eddy-induced velocity (EEIV, a scalar $\chi_\perp$), which is a speed with which eddies advect large-scale tracer contours. The EEIV effectively describes the mechanism of the eddy-driven frontogenesis: taking the passive temperature as an example, the eddies facilitate the advection of warmer (colder) water to the warm (cold) side of the front, squeeze the tracer contours, and thus sharpen the front. The same process is challenging to describe by eddy diffusion. For example, recent studies (Kamenkovich *et al.* 2021; Haigh *et al.* 2021*a*; Haigh & Berloff 2021) have found persistence of pairs of positive and negative eddy diffusivities ("polarity") that could be potentially responsible for stretching the contours and producing tracer filaments or fronts (Haigh & Berloff 2022). However, negative diffusivities are numerically unstable, and compensation with the large-scale advection cannot be guaranteed for an arbitrary tracer. In addition, either up- or down-gradient diffusion is associated with cross-contour mixing, which is incompatible with the contour-squeezing nature of the front. Thus, we argue that an advective model is more suitable for representing the eddy-driven frontogenesis.

The EEIV formulation has two main advantages over the originally proposed vector formulation of the eddy-induced velocity (EIV, χ, (Lu *et al.* 2022)). The first advantage is the reduced tracer dependence, which means less sensitivity of $\chi_{\perp}$ to initial tracer profiles and thus smaller bias in simulating different tracers. Since Lu *et al.* (2022) shows a reduced tracer dependence of χ compared to the eddy diffusivity, the EEIV $\chi_{\perp}$ also has clear advantages over the diffusivity in this regard. The second advantage is that the uncovered eddy-induced frontal sharpening can be readily enforced by specifying $\chi_{\perp}$ in coarse-resolution models. Our results show that the EEIV effectively reproduces the strength of the front for both tracers with very different initial distributions: the passive temperature and chemical tracers. The EIV framework is, however, less practical because the vector χ is nearly parallel to the tracer contours in the frontal region and only a small cross-contour (effective) component of χ matters. Thus, even small errors in χ may yield large bias in the component and thus the front.

An interesting finding of this study is that the EEIV with full spatiotemporal variability fails to guarantee the frontogenesis and instead leads to further deterioration of the front from the simulation without eddy forcing. This is because of the rapid loss of correlation between the meandering front and parameterized eddy forcing, which leads to chaotic sensitivity of the frontal evolution to eddy forcing. The main merit of our results is that successful eddy tracer parameterization can be achieved with simplified, rather than most complex, parameterization, as long as the most important properties of the eddy effects can be preserved. For example, in this study, the tracer front is formed by the squeezing of the near-zonal tracer contours by the EIVs in the north and south of the EJE. We managed to use a simplified profile of EEIV to capture this feature of EIV that matters for fronts and thus guaranteed the frontogenesis. However, identification of such essential features may not be always straightforward since it requires careful analysis of what properties (e.g. spatiotemporal structures) of eddy effects are most important for the specific ocean phenomenon of interest. Machine learning approaches can be promising in this regard since they can extract essential properties from complex fields and even discover new physical relations (Zanna & Bolton 2020; Partee *et al.* 2022; Ross *et al.* 2023).

To account for the partial compensation between eddy-driven and large-scale tracer advection in the frontal region, we propose a closure for EEIV by using the effective large-scale velocity (ELSV). The closure captures the partial balance between EEIV and ELSV in the frontal region: the EEIV sharpens the front while the ELSV tries to broaden it, and effectively reproduces the eddy-driven frontal sharpening in the tracer experiment. The coefficient in the closure, which quantifies the compensation, is likely to depend on the flow properties. Thus, for each implementation in a model, such as a general circulation model (OGCM), one will need to tune the coefficient to produce a reasonable ocean fronts in the specific flow. Systematic investigation of the turning is left for future work.

Note, however, that the closure is not a complete parameterization because the large-scale flow in this study is projected from the eddy-resolving flow, with eddy-driven momentum and mass fluxes, rather than simulated in the non-eddy-resolving model. The advantage of using this approach is that we can focus on the role of tracer eddy forcing without the ambiguity from biases in momentum and mass fluxes. The dynamic effects of eddies in the EJE region is very likely to be at least as important as the eddy forcing, because the flow resolved in a non-eddy-resolving model differs significantly from the projected one, as shown in figure 3. Progress has been made in understanding and representing this dynamic effect (e.g. Berloff

2005; Zanna *et al.* 2017; Berloff 2018; Guillaumin & Zanna 2021; Uchida *et al.* 2022), which is outside the scope of this study.

This study focuses on the significance of mesoscale eddies on the large-scale tracer front. Submesoscale currents, another key component of oceanic flows but missing in this study, can also contribute to the frontogenesis (McWilliams 2016). These three-dimensional currents usually manifest themselves as overturning cells associated with upwelling and downwelling that enhance the fronts in ocean surface. Note that mesoscale eddies can also induce a similar overturning circulation in the surfaced mixed layer (Li *et al.* 2016; Li & Lee 2017), which could be another mechanism for eddy-induced frontogenesis. The fronts characterized by vertical motions occurring on horizontal scales of O(1-10 km) and in the mixed layer, however, are absent in our model. Studies of the importance of different scales for large-scale fronts should be continued in more realistic settings, as they provide insights on frontal dynamics and development of eddy parameterization scheme for non-eddy-resolving ocean models.

Acknowledgments. We thank Pavel Berloff for comments on draft of this manuscript. We also thank Michael Haigh for helping configure the MOM6. We acknowledge the support of the NSF Grant 1849990. We acknowledge high-performance computing support from Cheyenne (doi:10.5065/D6RX99HX) and Derecho (doi:10.5065/qx9a-pg09) provided by NCAR's Computational and Information Systems Laboratory, sponsored by the NSF.

Declaration of interests. The authors report no conflict of interest.

Data availability statement. The source code of the MOM6 ocean model configured for this study is available at https://github.com/yueyanglu/MOM6-DG. The offline tracer model source code and analysis code are available at https://github.com/yueyanglu/mesoeddies_front. The offline tracer model outputs and diagnostics are available at https://doi.org/10.5281/zenodo.10051655. The raw high-resolution ocean model outputs are available upon request from the author.

Author ORCIDs. Yueyang Lu, https://orcid.org/0000-0003-3102-8519;
Igor Kamenkovich, https://orcid.org/0000-0001-6228-5599

Appendix A. Model Equations

Here we explain some terms in the momentum and continuity equations (2.1). More detailed description of MOM6 equations can be found in Yankovsky *et al.* (2022) and Zhang *et al.* (2023). The Montgomery potential M_k (2.1a) in layer k is

$$M_k = \sum_{i=1}^{k} g'_{i-1/2} \eta'_{i-1/2}, \tag{A 1}$$

where $g'_{i-1/2}$ is the reduced gravity at the upper interface of layer k and its value is prescribed (table 1), and the upper interface height of layer k is $\eta'_{k-1/2} = -D + \sum_{i=1}^{k} h_i$, $D = 4$ km is ocean depth. The wind stress $\boldsymbol{\tau}$ is

$$\tau_x = \frac{\tau_0}{2}\left[1 + \cos\left(\frac{2\pi(mx - y + L_y/2)}{(1+m)L_y}\right)\right], \tag{A 2a}$$

$$\tau_y = m\tau_x, \tag{A 2b}$$

where the tilt parameter $m = 0.1$. The reference profile for the relaxation of the upper layer thickness in (2.1b) is the layer thickness plus a sinusoidal function whose zero-crossing line overlaps the zero wind stress curl line:

$$h_r = H_1 + \Delta h \sin\left(\frac{2\pi(mx - y + L_y/2)}{(1+m)L_y}\right), \tag{A 3}$$

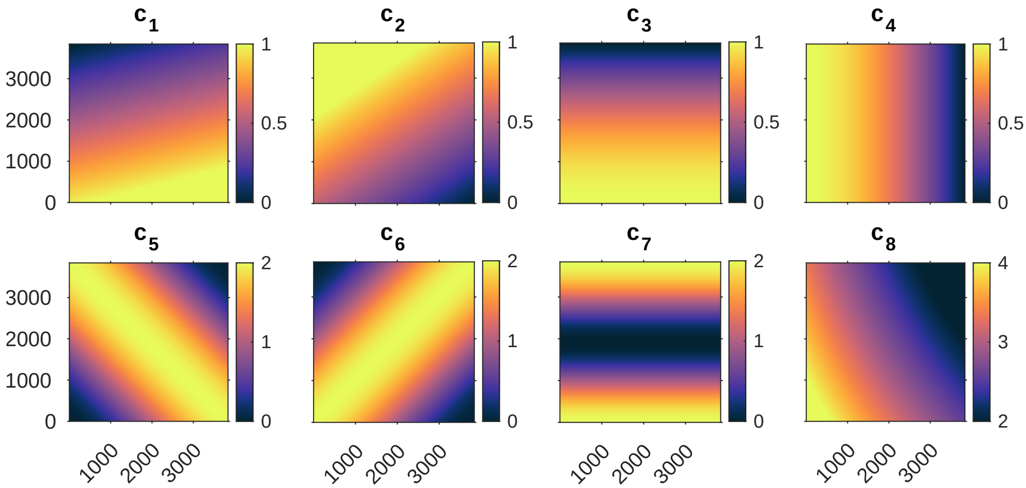

Figure 14: Initial distributions of the idealized tracers.

with $\Delta h = 150$ m.

Appendix B. Initial Distributions of Idealized Tracers

Besides the passive temperature and chemical tracers, this study also simulates eight additional idealized tracers. They are mainly used to evaluate the tracer dependence of the EEIV $\chi_\perp$ in section 3.3. Their concentrations are initialized with different horizontal distributions and are taken constant in the vertical direction (figure 14):

$$
\begin{aligned}
c_1 &= \frac{1}{\sqrt{17}}\left(\frac{x}{L_x} - 4\frac{y}{L_y} + 4\right), & c_2 &= \frac{1}{\sqrt{13}}\left(-2\frac{x}{L_x} + 3\frac{y}{L_y} + 2\right), \\
c_3 &= \cos\frac{\pi y}{2L_y}, & c_4 &= \cos\frac{\pi x}{2L_x}, \\
c_5 &= -\cos\left(\frac{\pi x}{L_x} + \frac{\pi y}{L_y}\right) + 1, & c_6 &= \cos\left(-\frac{\pi x}{L_x} + \frac{\pi y}{L_y}\right) + 1, \\
c_7 &= \cos\frac{2\pi y}{L_y} + 1, & c_8 &= 25 * \left[\frac{\left(0.4\frac{x}{L_x} - 1\right)^2}{9} + \frac{\left(0.4\frac{y}{L_y} - 1\right)^2}{16}\right],
\end{aligned}
\tag{B 1}
$$

where L_x and L_y are the domain sizes in the zonal and meridional directions, respectively.

Appendix C. Test of Offline Tracer Advection

To evaluate the accuracy of the offline tracer simulation, we perform both online and offline simulations of the passive temperature tracer on the high-resolution grid. The tracer is initialized on the first day of year 21. We use the spatial standard deviation of the tracer in a model layer to quantify the error (Kamenkovich & Garraffo 2022):

$$
SD(c) = \left[\frac{1}{V}\int c^2 h\,dxdy - \left(\int ch\,dxdy\right)^2\right]^{1/2}, \tag{C 1}
$$

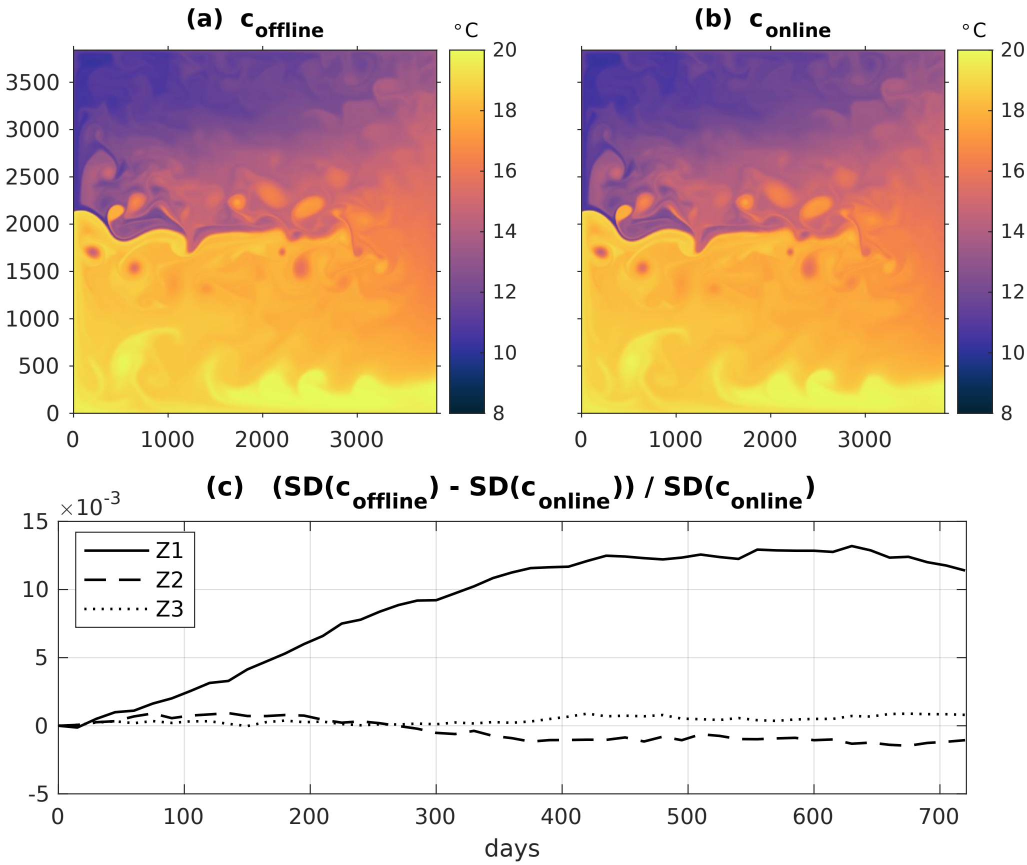

Figure 15: Passive temperature tracer solutions from the high-resolution (a) offline and (b) online simulations in the upper layer at day 365 year 22. (c) Time series of the relative bias e in the three layers.

where $V = \int h\, dxdy$ is the volume of the layer. The two solutions are indistinguishable from each other at the end of the 2-yr integration (figure 15). The relative bias, $e = (SD(c_{off}) - SD(c_{onl}))/SD(c_{onl})$, remain less than 1.5%. The bias is much smaller for the simulations on the coarse grid (not shown). Therefore, the errors due to the use of six-hourly mean fields are sufficiently small to warrant the use of the offline simulations.

Appendix D. Coarse Graining of the Mass Flux

The first step of defining the large-scale mass flux $\boldsymbol{U}_L$ (3.3) is to coarse grain the high-resolution mass flux $\boldsymbol{U}$. Since the divergence of mass flux determines the layer thickness and thus tracer concentration, we choose to preserve the divergence during the coarse graining. This is achieved by utilizing the Helmholtz decomposition as follows. The high-resolution mass flux $\boldsymbol{U}$ is first decomposed into its divergent and rotational components (Maddison *et al.* 2015):

$$\boldsymbol{U} = \nabla\phi + \hat{z} \times \nabla\psi, \tag{D 1}$$

$$\nabla \cdot \boldsymbol{U} = \nabla^2\phi, \qquad (\hat{z} \times \nabla) \cdot \boldsymbol{U} = \nabla^2\psi,$$

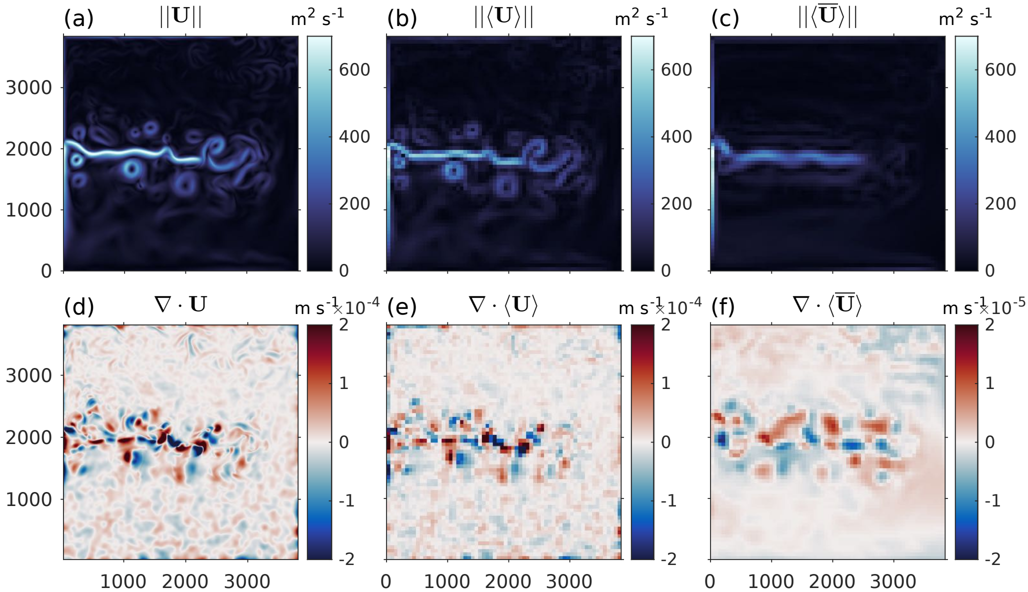

Figure 16: Norm of (a) the high-resolution mass flux, (b) the coarse-rained mass flux, and (c) the large-scale mass flux $\boldsymbol{U}_L$ (coarse-grained and time filtered), at day 120 year 21 in the upper layer. (d)-(f) Divergences of the mass fluxes in (a)-(c), respectively. Note the color scale in (f) is ten times smaller than in (d) and (e).

where ϕ is potential for the divergent component ($\nabla\phi$), ψ is streamfunction for the rotational component ($\hat{z}\times\nabla\psi$), $\hat{z}$ is the unit vector in the vertical direction, and $(\hat{z}\times\nabla)\cdot(\ldots) = (-\partial_y, \partial_x)$ is the horizontal curl operator.

We then coarse grain the flux divergence to get $\langle\nabla\cdot\boldsymbol{U}\rangle$. To get a corresponding divergent component, we solve the Poisson problem on the coarse grid with zero norm-flux boundary condition

$$\nabla_c^2\phi^c = \langle\nabla\cdot\boldsymbol{U}\rangle, \tag{D 2}$$

where ϕ_c is the potential for the divergent component ($\nabla_c\phi_c$) on the coarse grid. We also coarse grain ψ to get the streamfunction for the rotational component on the coarse grid

$$\psi_c = \langle\psi\rangle. \tag{D 3}$$

The coarse-grained mass flux is then defined as

$$\langle\boldsymbol{U}\rangle = \nabla_c\phi_c + \hat{z}\times\nabla_c\psi_c, \tag{D 4}$$

$$\nabla_c\cdot\langle\boldsymbol{U}\rangle = \nabla_c^2\phi_c = \langle\nabla\cdot\boldsymbol{U}\rangle, \qquad (\hat{z}\times\nabla_c)\cdot\langle\boldsymbol{U}\rangle = \nabla_c^2\psi_c.$$

Its divergence by definition equals the coarse-grained divergence of the high-resolution mass flux, which guarantees reasonable layer thickness and tracer solutions on the coarse grid. The coarse-grained mass flux also preserves the flow structure in $\boldsymbol{U}$, because the streamfunction for the rotational component of $\langle\boldsymbol{U}\rangle$ is directly projected from that of $\boldsymbol{U}$.

For a comparison, we attempted a simple way by coarse graining the zonal and meridional components of $\boldsymbol{U}$ separately. However, the resulting mass flux has a divergence more than ten times larger than the divergence of $\boldsymbol{U}$ and causes instabilities in the coarse-grid continuity and tracer simulation. This issue is due to the non-commutativity between discrete spatial-derivative operators and discrete coarse-graining (Mana & Zanna 2014). A more rigorous

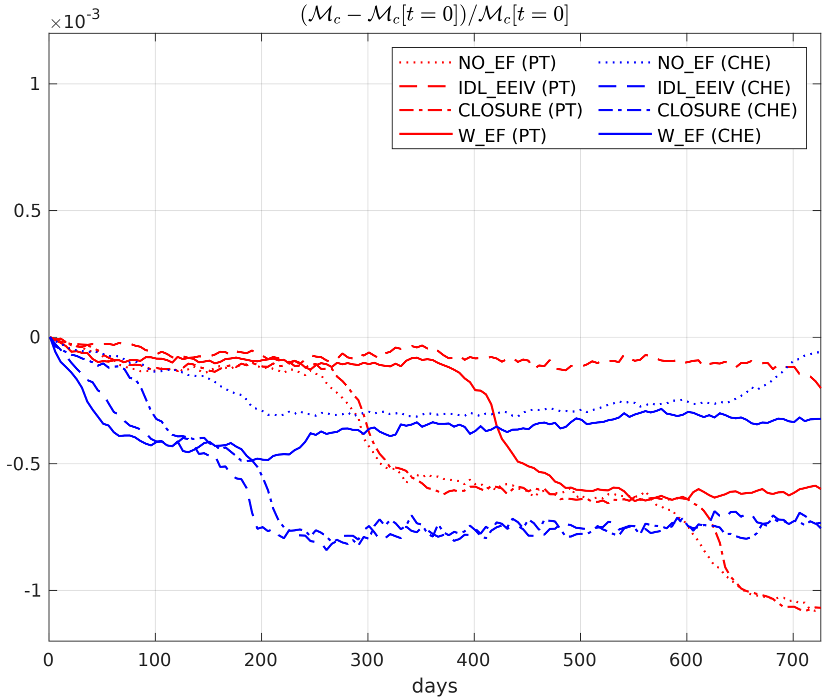

Figure 17: Evolution of the changes in the integrated tracer mass relative to the initial value from different experiments in the upper layer. Red is for the passive temperature tracer and blue is for the chemical tracer.

divergence-preserving coarse-graining method can be found in Patching (2022) but is not applied here due to its complexity.

The large-scale mass flux $\boldsymbol{U}_L$ is then obtained by time filtering $\langle \boldsymbol{U} \rangle$ with a 180-day window. Figure 16 shows its norm and divergence, as well as those of $\boldsymbol{U}$ and $\langle \boldsymbol{U} \rangle$. We see that the elongated jet extension is well retained in $\boldsymbol{U}_L$ and the divergences of $\langle \boldsymbol{U} \rangle$ and $\boldsymbol{U}_L$ do not exceed the high-resolution flux divergence. The time filtering eliminate the mesoscale structures (e.g. vortices) in $\langle \boldsymbol{U} \rangle$ (figures 16b-c). We conclude that the combination of coarse-graining and time averaging effectively remove the mesoscale variability in the flow.

Appendix E. Tracer Mass Conservation

To ensure the tracer conservation when applying the EEIV formulation (3.7), we add a correction to the local parameterized eddy forcing $\hat{\mathcal{D}}$ (Lu *et al.* 2022). The tracer solution c_* at a certain time step is given by

$$c_* = c_0 + \hat{\mathcal{D}} + w \left[\hat{\mathcal{D}} \right], \tag{E 1}$$

$$w = -\frac{|\hat{\mathcal{D}}|}{\left[|\hat{\mathcal{D}}| \right]} \tag{E 2}$$

where c_0 is the tracer at the last time step, the square brackets denote a global average of the layer thickness-weighted quantity: $[A] = \int Ah \, \mathrm{d}x\mathrm{d}y / \int h \, \mathrm{d}x\mathrm{d}y$, and the local weights w make the magnitude of the correction proportional to the amplitude of the local eddy forcing.

Tracer mass conservation requires $[c_*] = [c_0]$, which is satisfied by our choice of w

above. One can prove this by taking $[\cdots]$ of (E 1). Note that Lu *et al.* (2022) chose a simpler weight $w = 1$, which was also tested in this study and did not affect our conclusions. Such correction that modifies the parameterized forcing has been widely applied to stochastic parameterizations in the operational ECMWF models (e.g. Leutbecher 2017).

We present the changes of the globally integrated tracer inventory, $\mathcal{M}_c = \int ch\,\mathrm{d}x\mathrm{d}y$, relative to its initial value for both the passive temperature and chemical tracers in figure 17. The change in $\mathcal{M}_c$ from the IDL_EEIV and CLOSURE experiments remain in the same range ($< 0.1\%$) with that from the NO_EF and W_EF runs, confirming that the foregoing conservation modification works. Note that the total tracer inventory is not strictly conserved because of the relaxation surface boundary conditions, although such enforcement is straightforward to implement if desired (Lu *et al.* 2022).

REFERENCES

Adcroft, A. et al. 2019 The GFDL Global Ocean and Sea Ice Model OM4.0: Model Description and Simulation Features. *J. Adv. Model. Earth Syst.* **11** (10), 3167–3211.

Agarwal, N., Ryzhov, E., Kondrashov, D. & Berloff, P. 2021 Correlation-based flow decomposition and statistical analysis of the eddy forcing. *J. Fluid Mech.* **924**, A5.

Bachman, S. 2019 The GM+E closure: A framework for coupling backscatter with the Gent and McWilliams parameterization. *Ocean Modell.* **136**, 85–106.

Bachman, S., Fox-Kemper, B. & Bryan, F. 2015 A tracer-based inversion method for diagnosing eddy-induced diffusivity and advection. *Ocean Modell.* **86**, 1–14.

Bachman, S., Fox-Kemper, B. & Pearson, B. 2017 A scale-aware subgrid model for quasi-geostrophic turbulence. *J. Geophys. Res. Oceans* **122** (2), 1529–1554.

Bachman, Scott D., Fox-Kemper, Baylor & Bryan, Frank O. 2020 A Diagnosis of Anisotropic Eddy Diffusion From a High-Resolution Global Ocean Model. *J. Adv. Model. Earth Syst.* **12** (2).

Belkin, I., Cornillon, P. & Sherman, K. 2009 Fronts in Large Marine Ecosystems. *Prog. Oceanogr.* **81** (1-4), 223–236.

Berloff, P. 2005 On dynamically consistent eddy fluxes. *Dyn. Atmos. Oceans* **38** (3), 123–146.

Berloff, Pavel 2018 Dynamically consistent parameterization of mesoscale eddies. Part III: Deterministic approach. *Ocean Modell.* **127**, 1–15.

Berloff, P., Kamenkovich, I. & Pedlosky, J. 2009 A model of multiple zonal jets in the oceans: Dynamical and kinematical analysis. *J. Phys. Oceanogr.* **39** (11), 2711–2734.

Berloff, P., Ryzhov, E. & Shevchenko, I. 2021 On dynamically unresolved oceanic mesoscale motions. *J. Fluid Mech.* **920**, A41.

Cooper, F. & Zanna, L. 2015 Optimisation of an idealised ocean model, stochastic parameterisation of sub-grid eddies. *Ocean Modell.* **88**, 38–53.

D'Asaro, E., Lee, C., Rainville, L., Harcourt, R. & Thomas, L. 2011 Enhanced Turbulence and Energy Dissipation at Ocean Fronts. *Science* **332** (6027), 318–322.

England, M. H., Garçon, V. & Minster, J. 1994 Chlorofluorocarbon uptake in a world ocean model: 1. Sensitivity to the surface gas forcing. *J. Geophys. Res. Oceans* **99** (C12), 25215–25233.

Ferrari, R. 2011 A Frontal Challenge for Climate Models. *Science* **332** (6027), 316–317.

Gent, P. & McWilliams, J. 1990 Isopycnal Mixing in Ocean Circulation Models. *J. Phys. Oceanogr.* **20** (1), 150–155.

Gent, P., Willebrand, J., McDougall, T. & McWilliams, J. 1995 Parameterizing Eddy-Induced Tracer Transports in Ocean Circulation Models. *J. Phys. Oceanogr.* **25** (4), 463–474.

Grooms, I. 2016 A Gaussian-product stochastic Gent–McWilliams parameterization. *Ocean Modell.* **106**, 27–43.

Grooms, I. & Kleiber, W. 2019 Diagnosing, modeling, and testing a multiplicative stochastic Gent-McWilliams parameterization. *Ocean Modell.* **133**, 1–10.

Guillaumin, A. & Zanna, L. 2021 Stochastic-Deep Learning Parameterization of Ocean Momentum Forcing. *J. Adv. Model. Earth Syst.* **13** (9), e2021MS002534.

Haigh, M. & Berloff, P. 2021 On co-existing diffusive and anti-diffusive tracer transport by oceanic mesoscale eddies. *Ocean Modell.* **168**, 101909.

Haigh, M. & Berloff, P. 2022 On the stability of tracer simulations with opposite-signed diffusivities. *J. of Fluid Mech.* **937**, R3.

Haigh, M., Sun, L., McWilliams, J. & Berloff, P. 2021*a* On eddy transport in the ocean. Part I: The diffusion tensor. *Ocean Modell.* **164**, 101831.

Haigh, M., Sun, L., McWilliams, J. & Berloff, P. 2021*b* On eddy transport in the ocean. Part II: The advection tensor. *Ocean Modell.* **165**, 101845.

Haigh, M., Sun, L., Shevchenko, I. & Berloff, P. 2020 Tracer-based estimates of eddy-induced diffusivities. *Deep Sea Res. I: Oceanogr. Res. Pap.* **160**, 103264.

Haney, R. 1971 Surface Thermal Boundary Condition for Ocean Circulation Models. *J. Phys. Oceanogr.* **1** (4), 241–248.

Hewitt, H. et al. 2020 Resolving and Parameterising the Ocean Mesoscale in Earth System Models. *Curr Clim Change Rep* **6** (4), 137–152.

Hoskins, B. 1982 The Mathematical Theory of Frontogenesis. *Annu. Rev. Fluid Mech.* **14** (1), 131–151.

Kamenkovich, I., Berloff, P., Haigh, M., Sun, L. & Lu, Y. 2021 Complexity of Mesoscale Eddy Diffusivity in the Ocean. *Geophys. Res. Lett.* **48** (5).

Kamenkovich, I., Berloff, P. & Irina, R. 2019 Anisotropic and inhomogeneous eddy-induced transport in flows with jets. In *Zonal jets: Phenomenology, genesis, and physics*, pp. 437–449. Cambridge University Press.

Kamenkovich, I. & Garraffo, Z. 2022 Importance of Mesoscale Currents in Amoc Pathways and Timescales. *J. Phys. Oceanogr.* **52** (8), 1613–1628.

Kamenkovich, I., Garraffo, Z., Pennel, R. & Fine, R. 2017 Importance of mesoscale eddies and mean circulation in ventilation of the Southern Ocean. *J. Geophys. Res. Oceans* **122** (4), 2724–2741.

Kirtman, B. et al. 2012 Impact of ocean model resolution on CCSM climate simulations. *Clim. Dyn.* **39** (6), 1303–1328.

Leutbecher, M. et al. 2017 Stochastic representations of model uncertainties at ECMWF: state of the art and future vision. *Quart. J. Roy. Meteor. Soc.* **143** (707), 2315–2339.

Li, Q. & Lee, S. 2017 A Mechanism of Mixed Layer Formation in the Indo–Western Pacific Southern Ocean: Preconditioning by an Eddy-Driven Jet-Scale Overturning Circulation. *J. Phys. Oceanogr* **47** (11), 2755–2772.

Li, Q., Lee, S. & Griesel, A. 2016 Eddy Fluxes and Jet-Scale Overturning Circulations in the Indo–Western Pacific Southern Ocean. *J. Phys. Oceanogr* **46** (10), 2943–2959.

Lohmann, R. & Belkin, I. 2014 Organic pollutants and ocean fronts across the Atlantic Ocean: A review. *Progress in Oceanography* **128**, 172–184.

Lu, Y., Kamenkovich, I. & Berloff, P. 2022 Properties of the Lateral Mesoscale Eddy-Induced Transport in a High-Resolution Ocean Model: Beyond the Flux–Gradient Relation. *J. Phys. Oceanogr.* **52** (12), 3273–3295.

Maddison, J.R., Marshall, D.P. & Shipton, J. 2015 On the dynamical influence of ocean eddy potential vorticity fluxes. *Ocean Modell.* **92**, 169–182.

Mana, P. & Zanna, L. 2014 Toward a stochastic parameterization of ocean mesoscale eddies. *Ocean Modell.* **79**, 1–20.

McWilliams, J. 2016 Submesoscale currents in the ocean. *Proc. R. Soc. A* **472** (2189), 20160117.

McWilliams, J. 2021 Oceanic Frontogenesis. *Annu. Rev. Fluid Mech.* **13** (1), 227–253.

Meijers, A 2014 The Southern Ocean in the Coupled Model Intercomparison Project phase 5. *Phil. Trans. R. Soc. A.* **372** (2019), 20130296.

Minobe, S., Kuwano-Yoshida, A., Komori, N., Xie, S.-P. & Small, J. 2008 Influence of the Gulf Stream on the troposphere. *Nature* **452** (7184), 206–209.

Mudrick, S. 1974 A Numerical Study of Frontogenesis. *J. Atmos. Sci.* **31** (4), 869–892.

Nakamura, N. 1996 Two-Dimensional Mixing, Edge Formation, and Permeability Diagnosed in an Area Coordinate. *J. Atmos. Sci.* **53** (11), 1524–1537.

Parfitt, R., Czaja, A., Minobe, S. & Kuwano-Yoshida, A. 2016 The atmospheric frontal response to SST perturbations in the Gulf Stream region. *Geophys. Res. Lett.* **43** (5), 2299–2306.

Partee, S., Ellis, M., Rigazzi, A., Shao, A., Bachman, S., Marques, G. & Robbins, B. 2022 Using Machine Learning at scale in numerical simulations with SmartSim: An application to ocean climate modeling. *J. Comput. Sci.* **62**, 101707.

Patching, S. 2022 On divergence- and gradient-preserving coarse-graining for finite volume primitive equation ocean models. *Ocean Modell.* **170**, 101941.

Pedlosky, J. 1987 *Geophysical Fluid Dynamics*. Springer New York.

Redi, M. 1982 Oceanic Isopycnal Mixing by Coordinate Rotation. *J. Phys. Oceanogr.* **12** (10), 1154–1158.

Ross, A., Li, Z., Perezhogin, P., Fernandez-Granda, C. & Zanna, L. 2023 Benchmarking of Machine Learning Ocean Subgrid Parameterizations in an Idealized Model. *J. Adv. Model. Earth Syst.* **15** (1), e2022MS003258.

Rypina, I., Jayne, S., Yoshida, S., Macdonald, A. M., Douglass, E. & Buesseler, K. 2013 Short-term dispersal of Fukushima-derived radionuclides off Japan: modeling efforts and model-data intercomparison. *Biogeosciences* **10** (7), 4973–4990.

Rypina, I., Pratt, L. & Lozier, S. 2011 Near-Surface Transport Pathways in the North Atlantic Ocean: Looking for Throughput from the Subtropical to the Subpolar Gyre. *J. Phys. Oceanogr.* **41** (5), 911–925.

Ryzhov, E. & Berloff, P. 2022 On transport tensor of dynamically unresolved oceanic mesoscale eddies. *J. Fluid Mech.* **939**, A7.

Seo, H. et al. 2023 Ocean Mesoscale and Frontal-Scale Ocean–Atmosphere Interactions and Influence on Large-Scale Climate: A Review. *J. Climate* **36** (7), 1981–2013.

Shevchenko, I. & Berloff, P. 2015 Multi-layer quasi-geostrophic ocean dynamics in Eddy-resolving regimes. *Ocean Modell.* **94**, 1–14.

Siqueira, L. & Kirtman, B. 2016 Atlantic near-term climate variability and the role of a resolved Gulf Stream. *Geophys. Res. Lett.* **43** (8), 3964–3972.

Smagorinsky, J. 1963 General circulation experiments with the primitive equations: I. The basic experiment. *Mon. Weather Rev.* **91** (3), 99–164.

Small, J., deSzoeke, S.P., Xie, S.P., O'Neill, L., Seo, H., Song, Q., Cornillon, P., Spall, M. & Minobe, S. 2008 Air–sea interaction over ocean fronts and eddies. *Dyn. Atmos. Oceans* **45** (3-4), 274–319.

Small, J., Tomas, R. & Bryan, F. 2014 Storm track response to ocean fronts in a global high-resolution climate model. *Clim. Dyn.* **43** (3), 805–828.

Sun, L., Haigh, M., Shevchenko, I., Berloff, P. & Kamenkovich, I. 2021 On non-uniqueness of the mesoscale eddy diffusivity. *J. Fluid Mech.* **920**, A32.

Trias, F., Dabbagh, F., Gorobets, A. & Oliet, C. 2020 On a Proper Tensor-Diffusivity Model for Large-Eddy Simulation of Buoyancy-Driven Turbulence. *Flow Turbul. Combust.* **105** (2), 393–414.

Uchida, T., Deremble, B. & Popinet, S. 2022 Deterministic Model of the Eddy Dynamics for a Midlatitude Ocean Model. *J. Phys. Oceanogr.* **52** (6), 1133–1154.

Vallis, G. K. 2017 *Atmospheric and Oceanic Fluid Dynamics*. Cambridge University Press.

Waterman, S., Hogg, N. & Jayne, S. 2011 Eddy–Mean Flow Interaction in the Kuroshio Extension Region. *J. Phys. Oceanogr.* **41** (6), 1182–1208.

Waterman, S. & Jayne, S. 2011 Eddy-Mean Flow Interactions in the Along-Stream Development of a Western Boundary Current Jet: An Idealized Model Study. *J. Phys. Oceanogr.* **41** (4), 682–707.

Yankovsky, E., Zanna, L. & Smith, S. 2022 Influences of Mesoscale Ocean Eddies on Flow Vertical Structure in a Resolution-Based Model Hierarchy. *J. Adv. Model. Earth Syst.* **14** (11), e2022MS003203.

Zanna, L. & Bolton, T. 2020 Data-Driven Equation Discovery of Ocean Mesoscale Closures. *Geophys. Res. Lett.* **47** (17), e2020GL088376.

Zanna, L., Mana, P., Anstey, J., David, T. & Bolton, T. 2017 Scale-aware deterministic and stochastic parametrizations of eddy-mean flow interaction. *Ocean Modell.* **111**, 66–80.

Zhang, C., Perezhogin, P., Gultekin, C., Adcroft, A., Fernandez-Granda, C. & Zanna, L. 2023 Implementation and Evaluation of a Machine Learned Mesoscale Eddy Parameterization Into a Numerical Ocean Circulation Model. *J. Adv. Model. Earth Syst.* **15** (10), e2023MS003697.

Zhang, W. & Wolfe, C. 2022 On the Vertical Structure of Oceanic Mesoscale Tracer Diffusivities. *J. Adv. Model. Earth Syst.* **14** (6).